Research Square

Preprints are preliminary reports that have not undergone peer review.
They should not be considered conclusive, used to inform clinical practice,
or referenced by the media as validated information.

Phase Evolution and Selective Barium Titanate Localization in Poly(vinylidene fluoride) and Epoxidized Natural Rubber Blends with Tunable Mechanical and Dielectric Properties

Subhan Salaeh
Prince of Songkla University
Philippe Cassagnau
University of Lyon, Université Claude Bernard Lyon1, Ingénierie des Matériaux Polymères (IMP), UMR CNRS
Charoen Nakason
charoen.nakason@gmail.com
Prince of Songkla University

Research Article

Keywords: Poly(vinylidene fluoride), epoxidized natural rubber, barium titanate, phase morphology, dielectric properties

Posted Date: August 13th, 2026

DOI: https://doi.org/10.21203/rs.3.rs-10619449/v1

License: This work is licensed under a Creative Commons Attribution 4.0 International License.
Read Full License

Additional Declarations: No competing interests reported.

Phase Evolution and Selective Barium Titanate Localization in Poly(vinylidene fluoride) and Epoxidized Natural Rubber Blends with Tunable Mechanical and Dielectric Properties

Subhan Salaeh[1], Philippe Cassagnau[3] and Charoen Nakason[2]

[1]Department of Rubber Technology and Polymer Science, Faculty of Science and Technology, Prince of Songkla University, Pattani Campus, 94000, Thailand;

[2]Faculty of Science and Industrial Technology, Prince of Songkla University, Surat Thani Campus, 84000, Thailand, [3]University of Lyon, Université Claude Bernard Lyon1, Ingénierie des Matériaux Polymères (IMP), UMR CNRS, Villeurbanne, France

Abstract

Non-vulcanized blends of poly(vinylidene fluoride) (PVDF) with epoxidized natural rubber containing 50 mol% epoxide (ENR-50) in 80/20–20/80 wt% ratios were prepared by melt blending. The PVDF/ENR-50 blends at 80/20 and 50/50 were filled with 5 vol% barium titanate (BT). SEM analysis revealed a change in morphology from PVDF continuity to apparent co-continuity at 60/40–50/50, followed by ENR-50 continuity at higher ENR-50 content. Increasing the ENR-50 content reduced stiffness and tensile stress but increased extensibility, with elongation at break values of about 1000–2200% in the ENR-50-rich blends. Furthermore, the PVDF crystallization temperature increased from 135.8 °C in neat PVDF to 139.3 °C at the 50/50 composition, whereas normalized PVDF crystallinity decreased from 54.2% at 60/40 to 43.7% at 20/80 due to phase confinement. Relaxation peaks at −36 and −9 °C indicated phase separation with partial interface compatibility. The novelty lies in the identification of two-phase inversion boundaries and the correlation between phase continuity and mechanical, thermal, dynamic-mechanical, and dielectric behavior. Moreover, BT particles preferentially segregated to ENR-50, increasing the average size of ENR-50 domains in the

80/20 blend from 6.5 to 11.4 μm without altering PVDF continuity.

Keywords: Poly(vinylidene fluoride); epoxidized natural rubber; barium titanate; phase morphology; dielectric properties

1. Introduction

Polymer blending is an attractive and economical strategy for combining properties that are difficult to obtain with a single polymer. Most polymer pairs are thermodynamically immiscible because their high molecular weights produce a low entropy of mixing, while the enthalpy of mixing is often unfavorable [1]. Their performance therefore depends strongly on phase morphology, interfacial adhesion, domain size, and phase continuity [2, 3]. Morphology can be controlled through blend composition, phase viscosity and elasticity ratios, interfacial tension, mixing conditions, and the competition among domain deformation, breakup, and coalescence during processing [4, 5]. Although complete miscibility is rare, immiscible blends can exhibit useful engineering properties when the morphology is refined and stabilized and sufficient interfacial adhesion enables effective stress transfer [2, 6]. Compatibilization may involve block or graft copolymers, reactive blending that forms interfacial copolymers *in situ*, or favorable intermolecular interactions [2], while dynamic crosslinking can further stabilize thermoplastic/elastomer morphologies [7]. These approaches reduce interfacial tension, suppress coalescence, refine morphology, and improve adhesion without necessarily creating a homogeneous phase [8]. Interfacial stabilization may also arise from covalent or ionic bonding, hydrogen bonding, dipole–dipole interactions, or other specific associations [6, 9]. Even when localized at the interphase, such interactions can modify chain mobility and crystallization, thereby affecting the mechanical, dynamic mechanical, and dielectric behavior of phase-separated blends [10]. Depending on composition, rheology, interfacial tension, and

processing conditions, polymer blends may form matrix–droplet, fibrillar, lamellar, or co-continuous morphologies [4, 11].

In dispersed morphologies, the continuous matrix governs the macroscopic response, while the dispersed phase modifies it through reinforcement, toughening, or energy dissipation. In co-continuous morphologies, both phases form interconnected networks and simultaneously contribute to load transfer, deformation, transport, and other functional properties [3, 12]. Co-continuity typically exists over a finite composition range rather than at a single blend ratio, with its boundaries governed by phase volume fractions and rheological properties. Because continuity is three-dimensional, assignments from two-dimensional microscopy should ideally be confirmed by selective extraction, rheology, electrical conductivity, or three-dimensional imaging [13]. In thermoplastic–elastomer blends, co-continuous or sufficiently interconnected morphologies can balance thermoplastic processability with rubber-like flexibility. However, strict co-continuity is not essential, as the required morphology depends on the state of the rubber phase. Uncrosslinked blends may be dispersed, interconnected, or co-continuous, whereas dynamic vulcanization typically produces crosslinked rubber particles within a continuous thermoplastic matrix [14, 15]. These materials are industrially attractive because they combine rubber-like flexibility and elasticity at service temperatures with thermoplastic melt processability, reprocessability, and recyclability [16]. In non-vulcanized thermoplastic–rubber blends, the thermoplastic phase mainly provides stiffness, strength, and dimensional stability, while the rubber phase improves flexibility, extensibility, damping, and impact resistance. Final properties therefore depend on composition, phase morphology, and the ability of each phase to form continuous or sufficiently interconnected pathways for load transfer or deformation [3].

Natural rubber (NR), a renewable elastomer obtained from *Hevea* brasiliensis latex, consists mainly of *cis*-1,4-polyisoprene and exhibits excellent extensibility, resilience, fatigue

resistance, and strain-induced crystallization [17, 18]. However, its nonpolar nature causes it to interact weakly with polar thermoplastics, often leading to poor compatibility, phase separation, and weak interfacial adhesion [19, 20]. However, these limitations can be mitigated by various chemical modification routes, particularly epoxidation, in which some carbon–carbon double bonds are converted into polar oxirane rings to form epoxidized natural rubber (ENR) [21]. In this case, increasing epoxide content enhances polarity, resistance to oil and gas permeation, wet grip, and interactions with polar polymers and fillers, while preserving NR's renewable origin and elastomeric flexibility [21–23]. Low to moderate epoxide contents preserve sufficiently long cis-1,4-isoprene sequences for strain-induced crystallization, whereas higher epoxidation disrupts these sequences and suppresses crystallization but enhances polarity, glass transition temperature, intermolecular interactions, and compatibility with polar materials [22, 24, 25]. ENR has therefore been widely used as an elastomeric, toughening, or compatibilizing agent in blends with various polymers, including polyamides [26], poly(vinyl chloride) [27], thermoplastic polyurethane [28], poly(lactic acid) [29], and poly(vinylidene fluoride) [30]. With suitable control of interfacial structure and network architecture, ENR-based materials can be designed for dielectric actuation, flexible sensing, shape-memory behavior, and other multifunctional applications [30–32].

Poly(vinylidene fluoride) (PVDF) is a semicrystalline thermoplastic fluoropolymer composed of repeating –CH_2–CF_2– units, combining good mechanical properties, chemical and weather resistance, thermal stability, melt processability, and relatively high dielectric permittivity [33, 34]. PVDF can crystallize in several polymorphs, including the nonpolar α phase and polar β, γ, and δ phases, which differ in chain conformation and dipole arrangement [33, 35]. Because of the large dipole moment of its C–F bonds, PVDF can exhibit ferroelectric, piezoelectric, and pyroelectric behavior when polar phases are formed and properly oriented or poled [35]. It is therefore widely studied for capacitors, sensors, actuators, energy harvesters,

membranes, and flexible electronic devices [34, 35]. The alternating CF_2 units give PVDF a dielectric permittivity higher than that of many conventional polymers, although neat PVDF remains inadequate for some compact capacitors, flexible sensors, actuators, and electromechanical devices. Therefore, incorporating high-permittivity ferroelectric barium titanate ($BaTiO_3$ or BT) is a common strategy to enhance the effective permittivity through BT polarization and interfacial polarization at polymer–ceramic interfaces [36, 37]. BT is attractive because of its high dielectric response, ferroelectricity, chemical stability, and lead-free composition. PVDF/BT composites have therefore been widely investigated for dielectric, piezoelectric, and energy-harvesting applications. Their performance depends on BT particle size and morphology, surface treatment, dispersion, loading, interfacial interactions, electroactive phase formation, porosity, and dielectric breakdown strength [38]. Although BT increases permittivity, high loadings may cause aggregation, interfacial defects, dielectric loss, electric-field concentration, excessive stiffening, and reduced breakdown strength and deformability. Therefore, improved permittivity alone does not ensure better energy-storage or actuation performance; BT distribution and polymer–ceramic interfacial structure are also critical [37, 39]. Blending PVDF with other polymers allows tailoring stiffness, toughness, crystallization behavior, damping characteristics, processability, and dielectric properties. PVDF blends may be miscible, partially miscible, or phase-separated, depending on the nature of the second polymer. For instance, a PVDF/PMMA blend exhibits a composition-dependent miscible system due to specific interactions between PMMA carbonyl groups and PVDF chains [40], whereas many other PVDF/elastomer blends remain phase-separated and require favorable interfacial interactions or compatibilization [41, 42]. In the PVDF/NR blends, an intrinsically incompatible blend was observed because of their large polarity difference. However, chemically modified NR, such as PMMA-grafted NR, can improve compatibility and enhance interfacial adhesion, while ENR provides a polar rubber phase capable of

interacting directly with PVDF [43]. Furthermore, amino acid–modified fluorocarbon elastomer has also been used as a reactive compatibilizer for PVDF/ENR-50 blends, refining the morphology and improving the mechanical performance [30]. ENR epoxide content, blend composition, and dynamic vulcanization strongly affect PVDF/ENR morphology and properties. At a 50/50 ratio, non-vulcanized PVDF/ENR-50 showed a finer co-continuous morphology than PVDF/ENR-25, indicating stronger interfacial interactions at higher epoxide content [44]. Dynamic vulcanization of PVDF/ENR-50 with phenolic resin further refined morphology and improved tensile properties and elastic recovery, while mechanical, thermal, dynamic-mechanical, and dielectric behavior remained dependent on composition, curing conditions, and filler content [45, 46].

Previous studies have mainly focused on limited compositions, compatibilized blends, or dynamically vulcanized systems. Therefore, this work systematically investigates non-vulcanized PVDF/ENR-50 blends over the 80/20–20/80 composition range to clarify how composition and phase continuity affect morphology, PVDF crystallization, tensile behavior, damping, and dielectric polarization. The 80/20 and 50/50 blends, representing PVDF-continuous and apparently co-continuous morphologies, respectively, were further filled with 5 vol% barium titanate (BT). The main novelty is demonstrating that selectively localized BT acts not only as a high-permittivity filler but also as a morphology-controlling component, thereby regulating stiffness, extensibility, damping, and dielectric behavior. These findings support the design of flexible dielectric, sensing, actuation, vibration-damping, and low-load electromechanical materials through control of composition, phase continuity, and filler localization.

2. Experimental

2.1 Materials

Poly(vinylidene fluoride) or PVDF (Kynar 740, M_w = 282,000 g/mol) was purchased from Arkema, France. Epoxidized natural rubber (ENR) with 50 mol% epoxide or ENR-50, Epoxyprene 50, was manufactured by Muang Mai Guthrie Co., Ltd., Surat Thani, Thailand. Barium titanate powder was purchased from Aesar GmbH (Germany). Wingstay L (Eliokem lnc, OH, USA) was used as an antioxidant.

2.2 Preparation of Blends and BT Composites

PVDF/ENR-50 blends with various proportions (80/20, 70/30, 60/40, 50/50, 40/60, 30/70, and 20/80 wt%) were prepared using a simple, non-vulcanized melt-blending technique at 180°C in an internal mixer (HAAKE Rheomix R600, Thermo Fisher Scientific Co., Ltd., Karlsruhe, Germany) with a mixing capacity of 50 cm^3 and a rotor speed of 50 rpm. The mixing process began with PVDF, which was mixed for 3 min until it melted. ENR-50 and Wingstay L antioxidant were then added, and mixing continued for an additional 5 min, giving a total mixing time of 8 min before the blend was discharged from the mixing chamber.

PVDF/ENR-50 blends with ratios of 80/20 and 50/50 wt% were then used to prepare blend composites by loading them with 5 v% BT, using the same mixing procedure described above. BT particles were added to the mixing chamber after 8 min of mixing, and mixing continued for another 7 min, for a total mixing time of 15 min. Blends with and without BT were then fabricated into thin sheets approximately 1 mm thick by compression molding (Polystat 200 T, Servitec Maschinenservice GmbH, Wustermark, Germany) at 180°C for 15 min. These sheets were subsequently used for testing and characterization of the blends.

2.3 Morphological properties

Morphological characterization was performed using a scanning electron microscope (SEM), specifically an FEI Quanta 400 instrument (FEI Company, Oregon, USA). The primary objective was to investigate phase development in blends with various compositions, both with and without BT. Fresh fracture surfaces were prepared by cryogenic fracturing in liquid nitrogen. For blends containing ENR-50 as the minor phase, the ENR-50 phase was selectively removed by extraction in toluene at room temperature for 72 h. However, blends with high ENR-50 contents were severely damaged by toluene extraction, making SEM observation impractical. Therefore, for blends in which ENR-50 was the major phase, the PVDF phase was selectively etched by extraction in dimethylformamide (DMF) at room temperature. After extraction, the samples were gently dried in a hot-air oven at 70 °C for 48 h to remove residual solvent. The dried fracture surfaces were subsequently sputter-coated with a thin layer of gold and examined by SEM.

2.4 Mechanical Properties

The tensile properties of PVDF/ENR-50 blends with different proportions, with and without BT filler, were determined using an MTS QTest 25 universal tensile testing machine (MTS Systems Corporation, North Carolina, USA). The measurements were performed at a crosshead speed of 500 mm/min in accordance with ISO 37. Tension-set measurements were carried out in accordance with ISO 2285. The specimens were stretched to 100% elongation at room temperature and held at this deformation for 10 min. They were then released, and the residual change in specimen dimensions was determined. The hardness of the samples was measured using a Shore A durometer in accordance with ISO 7619.

2.5 Differential scanning calorimetry (DSC)

A differential scanning calorimeter, DSC 2920 TA instrument (TA Instruments, New Castle, USA), was used to determine the thermal properties of neat PVDF and PVDF/ENR-50 blends, specifically the crystallization temperature (T_c) and melting temperature (T_m). Approximately 10 mg of each sample was hermetically sealed in an aluminum pan. Measurements were conducted under a helium atmosphere at a heating rate of 10 °C/min over a temperature range from −90 to 200 °C. The samples were maintained at 200 °C for 10 min to erase their prior thermal histories and were subsequently cooled from 200 to −90 °C at a cooling rate of 10 °C/min. The PVDF-normalized degree of crystallinity in the blends was calculated from the melting enthalpy using the following equation:

$$X_c(\%) = \frac{\Delta H_m (m_c / m_p)}{\Delta H_o} x100 \qquad (1)$$

where X_c is the degree of crystallinity of the PVDF phase, ΔH_m is the measured melting enthalpy of the sample, ΔH_0 is the theoretical melting enthalpy of 100 % crystalline PVDF (104.5 J/g) [47], m_c is the total mass of the sample and m_p is the mass of PVDF in the blend.

2.6 Dynamic mechanical properties (DMA)

The dynamic mechanical properties of the samples were characterized using a dynamic mechanical analyzer (DMA), TA Instruments model Q800 (TA Instruments, New Castle, DE, USA). Measurements were performed in tension mode over a temperature range from −90 to 100 °C at a fixed oscillation frequency of 1 Hz. The storage modulus (E') and loss tangent (tan δ) were recorded as functions of temperature. The storage modulus was used to evaluate the temperature-dependent stiffness and elastic response of the samples, whereas the tan δ curves

were used to assess molecular relaxation behavior and determine the glass-transition temperatures from the corresponding peak positions.

2.7 Dielectric properties

The dielectric properties of the PVDF/ENR blends with and without BT were measured by broadband dielectric spectroscopy (Novocontrol, Hundsangen, Germany) over a frequency range from 10^{-1} to 10^{7} Hz at room temperature. Aluminum electrodes were vapor-deposited onto both sides of each sample before the dielectric properties were determined.

3. Results and discussion

3.1 Effects of PVDF/ENR-50 blend composition

3.1.1Morphological properties

Figure 1 shows the etched morphologies of non-vulcanized PVDF/ENR-50 blends over the composition range 80/20–20/80 wt%. For the 80/20–50/50 blends shown in Figures 1(a–d), the ENR-50 phase was preferentially extracted with toluene for 72 h at room temperature. The dark cavities and channels in these micrographs correspond to regions originally occupied by ENR-50, while the remaining solid structure is predominantly PVDF. For the ENR-50-rich blends containing more than 50 wt% ENR-50, namely the 40/60, 30/70, and 20/80 blends in Figures 1(e–g), extraction of the major ENR-50 phase caused severe structural damage. Consequently, PVDF was preferentially extracted using DMF. The cavities in Figures 1(e–g) represent the removed PVDF phase, whereas the remaining solid framework corresponds predominantly to ENR-50. This difference in etching procedure must be considered when comparing morphologies across the entire composition range. In the 80/20 PVDF/ENR-50 blend [Figure 1(a)], elongated ENR-50-derived cavities are distributed within a continuous PVDF matrix, indicating a typical PVDF-continuous/ENR-50-dispersed morphology. The pronounced elongation of the ENR-50 domains suggests that the soft rubber phase underwent

substantial deformation under the shear field generated during melt mixing. When the ENR-50 content increases to 30 wt% [Figure 1(b)], the extracted ENR-50 domains appear finer, more numerous, and more closely spaced than those in the 80/20 blend, with some neighboring domains showing partial interconnection. This morphology suggests an increased probability of domain contact and coalescence, indicating the progressive development of ENR-50 continuity. Thus, the 70/30 PVDF/ENR-50 blend may approach the first boundary of the co-continuous region, where the morphology begins to evolve from a dispersed ENR-50 phase in a continuous PVDF matrix toward an interconnected structure of both phases [Figure 1(b)]. At a PVDF/ENR-50 ratio of 60/40 [Figure 1(c)], the ENR-50-derived cavities form an extensive interconnected network, while the residual PVDF phase also remains continuous. This morphology can therefore be classified as predominantly co-continuous phase structure. At the equimass composition of 50/50 [Figure 1(d)], highly elongated, oriented PVDF-rich ligaments are separated by continuous ENR-50-derived channels. The pronounced interpenetration of the two phases suggests that both PVDF and ENR-50 form continuous pathways. This preferential orientation may arise from shear-induced deformation and stretching during mixing, particularly when the phase fractions are comparable and neither component occurs exclusively as isolated droplets. Therefore, SEM images in Figures 1(c) and 1(d) can be considered the principal apparent co-continuous region. Nevertheless, it is noted that because the SEM micrographs represent two-dimensional sections of selectively etched specimens, this interpretation should be regarded as morphological evidence rather than definitive confirmation of three-dimensional co-continuity [3].

With a further increase in ENR-50 content, a marked morphological change is observed at 40/60 PVDF/ENR-50 [Figure 1(e)], for which the PVDF phase was selectively extracted using DMF. The predominantly rounded, closely spaced, and occasionally elongated cavities therefore correspond to the removed PVDF phase, whereas the surrounding solid framework

represents ENR-50. The limited interconnection among the PVDF-derived cavities suggests that PVDF progressively loses continuity and exists mainly as highly deformed or partially coalesced domains. In contrast, the continuous ENR-50 framework confirms that ENR-50 has become the dominant matrix phase. This composition can therefore be considered close to the second phase inversion boundary of the co-continuous region, where the morphology transitions from co-continuous to an ENR-50-matrix/PVDF-dispersed structure. At 30/70 PVDF/ENR-50 [Figure 1(f)], the extracted PVDF domains become more isolated, rounded, and relatively uniformly distributed within the continuous ENR-50 matrix, indicating that phase inversion to an ENR-50-continuous morphology is essentially complete.

Further decreasing the PVDF content to 20 wt% [Figure 1(g)] results in finer, more widely separated PVDF-derived cavities. The reduced domain size and connectivity are associated with the lower PVDF phase fraction, which decreases the probability of domain collision and coalescence during mixing. The predominantly rounded cavities also indicate that interfacial tension increasingly promotes shape relaxation when PVDF is present as the minor dispersed phase. Therefore, the morphology evolves through the following sequence: PVDF-continuous/ENR-50-dispersed → interconnected and apparently co-continuous PVDF/ENR-50 → ENR-50-continuous/PVDF-dispersed. Accordingly, the two observed phase-inversion events can be described more precisely as the two boundaries of the co-continuous region. The first boundary occurs approximately between the 70/30 and 60/40 blends, where ENR-50 changes from isolated or partially interconnected domains into an apparently continuous network. The second boundary occurs between the 50/50 and 40/60 blends, where PVDF progressively loses continuity and ENR-50 becomes the principal continuous phase.

The relatively broad co-continuous region may arise from the combined effects of blend composition, viscosity and elasticity ratios, interfacial tension, and the competition among domain deformation, breakup, and coalescence during melt mixing [48, 49]. Because

different phases were selectively extracted on the two sides of the composition range, direct comparison of cavity dimensions between Figures 1(d) and 1(e) should be made with caution. Toluene and DMF may induce different degrees of swelling, shrinkage, or interfacial damage. Nevertheless, the systematic changes in domain connectivity and matrix continuity provide clear qualitative evidence of phase separation and clearly identify the two phase-inversion boundaries of the co-continuous region in the PVDF/ENR-50 blends.

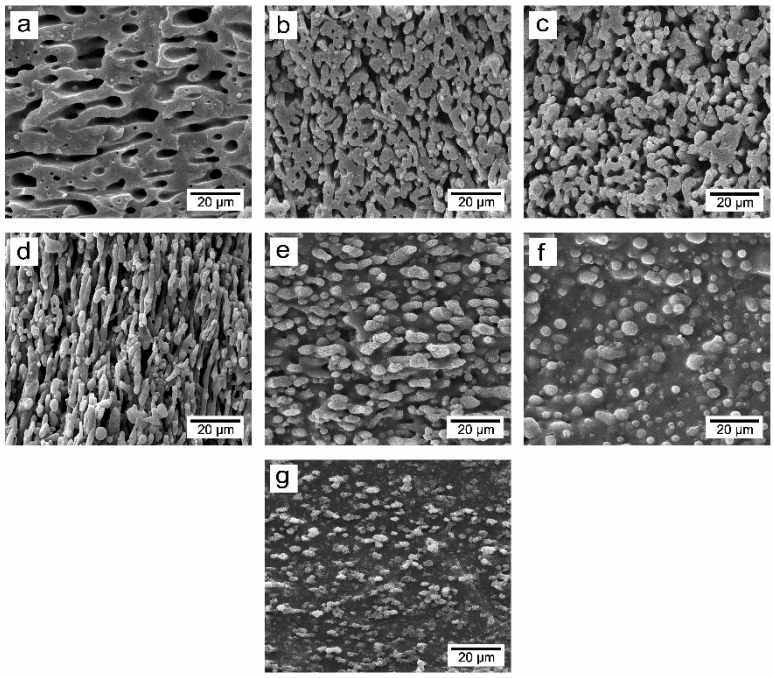


Figure 1. SEM micrographs of unvulcanized PVDF/ENR-50 blends with different blend ratios: (a) 80/20, (b) 70/30, (c) 60/40, (d) 50/50, (e) 40/60, (f) 30/70, and (g) 20/80 wt%.

Figure 2 schematically illustrates the proposed interfacial structure of the PVDF/ENR-50 blends. Although the blends remain phase separated, polar interactions between the oxirane- or hydroxyl-containing groups of ENR-50 and the dipolar PVDF chains may improve interfacial adhesion and partially stabilize the deformed phase morphology. Such interactions may reduce rapid domain retraction and coalescence during melt mixing, contributing to the relatively fine and elongated ENR-50 domains observed in the PVDF-rich blends in Figures

1(a) and 1(b). As the ENR-50 content increases, the reduced distance between neighboring rubber domains promotes their contact and interconnection, resulting in the apparently co-continuous morphologies observed at 60/40 and 50/50 PVDF/ENR-50 [Figures 1(c) and 1(d)]. The proposed interactions are expected to occur mainly within the amorphous PVDF regions and at the PVDF/ENR-50 interface rather than inside the tightly packed PVDF crystalline lamellae. However, the overall morphology remains controlled by blend composition, viscosity ratio, interfacial tension, and the competition between domain breakup and coalescence during mixing [47, 49]. Therefore, the schematic represents a possible molecular explanation for the improved interfacial compatibility and morphological stability, but it does not demonstrate complete miscibility or directly confirm hydrogen bonding.

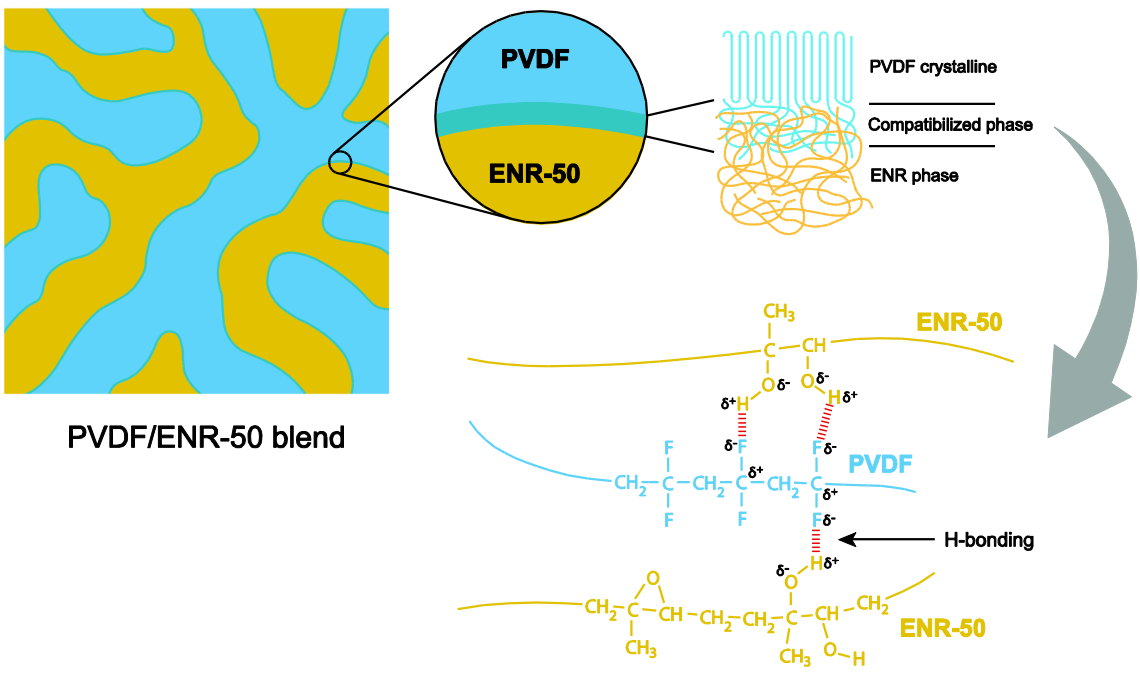


Figure 2. Schematic representation of the proposed morphology and possible interfacial interactions in PVDF/ENR-50 blends.

3.1.2 Mechanical properties

Tensile measurements, tension set, and hardness tests were carried out to determine the mechanical properties of the PVDF/ENR-50 blends, as shown in Figures 3 and 4. Figure 3 shows the stress–strain curves of the blends at various blend ratios. It can be seen that significant differences in deformation behavior occurred as the ENR-50 content increased. Specifically, the 80/20 PVDF/ENR-50 blend exhibited the highest initial slope, corresponding to the highest Young's modulus and the highest tensile stress, but the lowest strain at break (elongation at break). This indicates that the mechanical response was dominated by the stiffness of the PVDF matrix, which is consistent with the SEM-based morphology shown in Figure 1(a), where the ENR-50 phase exists mainly as isolated, elongated domains within a continuous PVDF phase. At this low rubber content, the widely separated ENR-50 domains cannot form an interconnected pathway for cooperative deformation. Consequently, stress is carried mainly by the continuous PVDF phase, and the blend retains a plastic-like response.This interpretation is consistent with the critical interparticle-distance concept, which states that widely separated rubber domains are less effective in promoting extensive deformation of the matrix [50]. Increasing the ENR-50 proportion progressively reduced the tensile stress and increased the deformation at break (Figure 3). For the 70/30 PVDF/ENR-50 blend, the reduction in tensile stress and the increase in extensibility correspond to the finer, more numerous, and more closely spaced ENR-50 domains observed in Figure 1(b). The reduced interdomain distance allows the rubber phase to participate more effectively in deformation, although PVDF remains the principal continuous matrix. When the ENR-50 content was increased to 40 wt% and above, the blends displayed markedly greater deformation and lower initial stiffness, reflecting a progressive transition from PVDF-dominated, plastic-like behavior to rubber-dominated, elastomer-like behavior. This change is associated not only with the increasing proportion of the soft ENR-50 phase but also with the morphological

evolution from isolated rubber domains to interconnected and apparently co-continuous structures, as observed in Figures 1(c) and 1(d). Therefore, the 60/40 PVDF/ENR-50 blend retained relatively high tensile stress while exhibiting a substantial increase in deformation compared with blends with lower rubber contents, such as the 80/20 and 70/30 blends. This response is consistent with the apparent co-continuous morphology observed in Figure 1(c), in which the continuous PVDF phase still serves as an effective stress-bearing component, while the interconnected ENR-50 phase contributes flexibility and facilitates large-scale deformation. This behavior matches the main characteristics of a thermoplastic elastomer (TPE), combining the load-bearing capability and processability of a plastic phase with the flexibility and extensibility of an elastomeric phase. Moreover, at the equal-mass blend proportion of 50/50 composition, the blend exhibited intermediate tensile stress together with considerably greater extensibility, revealing the apparent co-continuous morphology shown in Figure 1(d), which allows both phases to contribute to the mechanical response. In this circumstance, the PVDF-continuous network provides stiffness and facilitates load transfer, whereas the continuous ENR-50 phase accommodates deformation and enhances flexibility. Therefore, co-continuous morphologies can influence mechanical behavior differently from conventional droplet–matrix structures at low ENR-50 contents, because both components participate in stress transfer and deformation [47, 51].

In Figure 3, when the ENR-50 content exceeded 50 wt%, the tensile stress declined sharply, whereas the deformation at break increased markedly to approximately 1000–2200%. This behavior may coincide with the second phase inversion boundary observed in Figure 1(e), where ENR-50 becomes the dominant continuous matrix and PVDF progressively loses its continuity. With increasing rubber content to form the 30/70 and 20/80 PVDF/ENR-50 blends, the PVDF phase is present mainly as isolated dispersed domains within the continuous ENR-50 matrix [Figures 1(f) and 1(g)]. Consequently, the continuous stress-bearing contribution of

PVDF is substantially reduced, resulting in low tensile stress but very high flexibility and extensibility. Nevertheless, the exceptionally large deformation of the ENR-50-rich blends should be interpreted in the context of their non-vulcanized structure. In the absence, or at low contents, of a permanent chemically crosslinked network, the resistance of the ENR-50 phase to chain slippage, viscous flow, and irreversible deformation arises mainly from molecular entanglements and physical intermolecular interactions [52]. The dispersed or weakly interconnected PVDF domains may provide additional physical constraints on the deformation and mobility of the ENR-50 chains, although the magnitude of this reinforcement depends on the domain morphology and interfacial adhesion [53]. Therefore, the low tensile strength of these compositions reflects the limited network strength of the uncrosslinked, rubber-rich matrix. Nevertheless, blends exhibiting an apparently co-continuous phase morphology still provide a useful balance of strength, flexibility, and elastic recovery because the continuous PVDF phase contributes mechanical reinforcement and dimensional stability, whereas the interconnected ENR-50-rich phase enables extensive deformation. This combination of properties may be suitable for low-load, flexible applications, including soft protective sheets, flexible liners, vibration-damping components, cushioning materials, flexible seals, and other products requiring high extensibility rather than high structural strength.

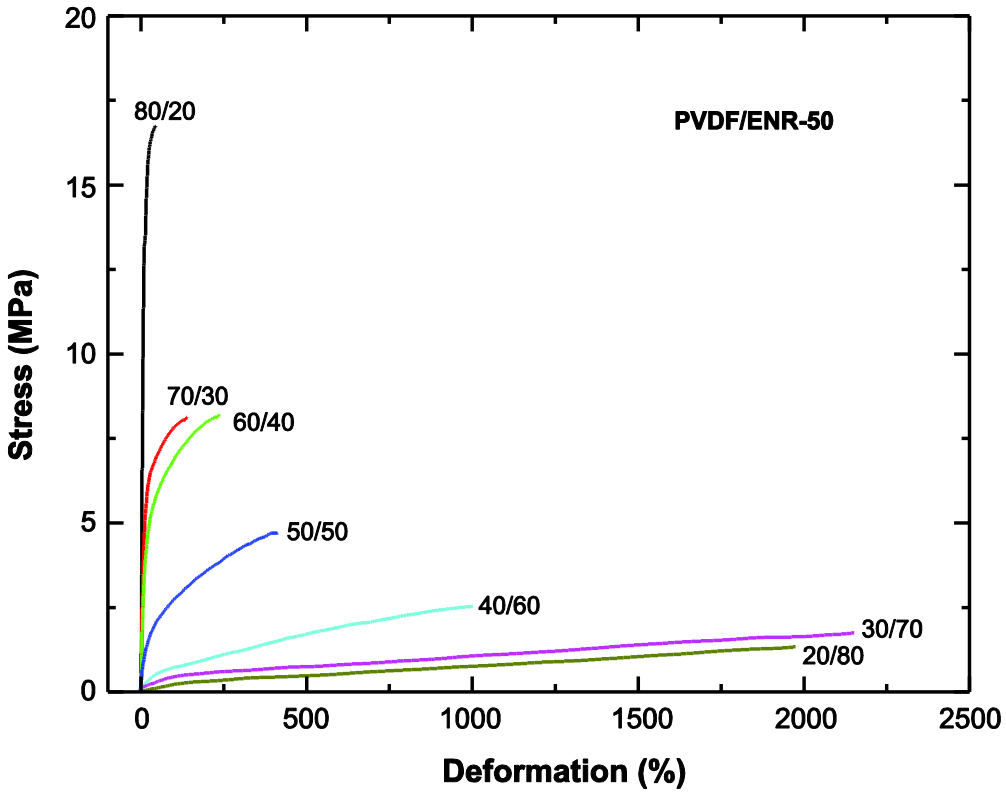


Figure 3. Stress–strain curves of PVDF/ENR-50 blends with different blend ratios.

Figure 4 shows the hardness and tension-set values as functions of ENR-50 content. Both hardness and tension set decreased progressively with increasing ENR-50 content. The reduction in hardness results primarily from replacing the stiff, semicrystalline PVDF phase with the softer, more mobile ENR-50 phase. This decrease is therefore consistent with the reduction in the initial slope of the stress–strain curves, corresponding to Young's modulus, shown in Figure 3. The phase morphology also contributes to this behavior. In the PVDF-rich blends, the continuous PVDF matrix restricts deformation and results in relatively high hardness. As the ENR-50 domains become increasingly interconnected and eventually form the continuous matrix, the resistance to indentation decreases markedly. The more pronounced reduction in hardness in the range of 40–60 wt% ENR-50 corresponds approximately to the apparent co-continuous and phase-inversion region identified in Figure 1.

In Figure 4, the decrease in tension set indicates that the blends recovered a greater proportion of their original dimensions after being released from 100% extension. The tension set of the 80/20 and 70/30 PVDF/ENR-50 blends could not be determined because their elongations at break were less than 100%. The improved recovery with increasing ENR-50 content is associated with the increasing proportion and continuity of the rubbery ENR-50 phase, which can undergo more extensive reversible chain rearrangement than the rigid PVDF phase. Nevertheless, the decrease in tension set should not be interpreted as evidence of the formation of a chemically crosslinked elastic network. In these non-vulcanized blends, shape recovery arises mainly from molecular entanglements, intermolecular interactions (Figure 2), and physical constraints imposed by the two-phase morphology. Although the ENR-50-rich blends exhibited very high extensibility and comparatively low tension set, their tensile stresses were considerably lower because the soft ENR-50 phase formed the principal continuous matrix, while the PVDF phase no longer provided a continuous load-bearing network. Among the investigated compositions, the 50/50 PVDF/ENR-50 blend provided a comparatively favorable balance of tensile stress, extensibility, hardness, and elastic recovery. This balance is closely associated with its apparent co-continuous morphology, in which the PVDF phase contributes strength and dimensional stability, whereas the ENR-50 phase provides flexibility and recovery. However, the optimum composition ultimately depends on the required balance between load-bearing capability and elastomeric deformation for a specific application.

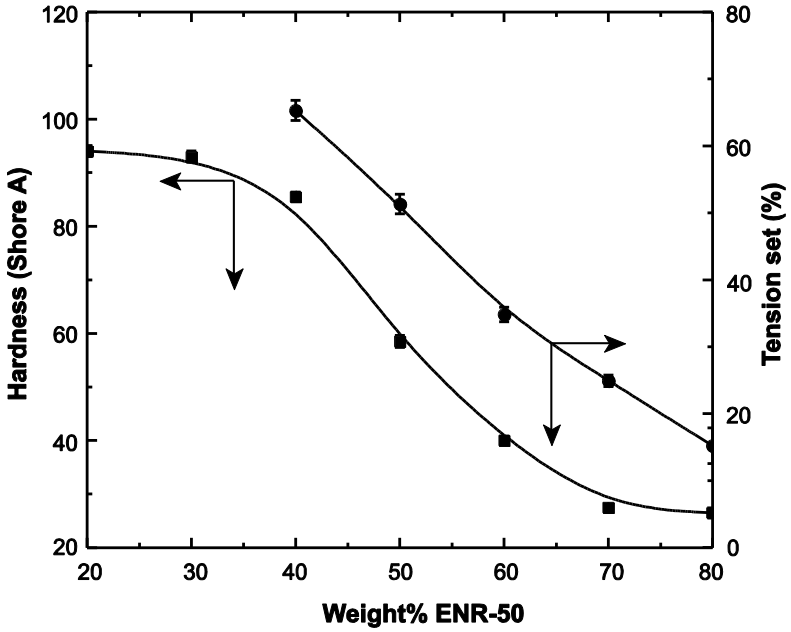


Figure 4. Hardness and tension set of PVDF/ENR-50 blend as a function of ENR-50 content in the blends.

3.1.3 Differential scanning calorimetry (DSC)

Figure 5 shows the DSC cooling and subsequent heating thermograms of neat PVDF and the non-vulcanized PVDF/ENR-50 blends, while Table 1 summarizes the crystallization peak temperature (T_c), full width at half maximum of the crystallization exotherm (*FWHM*), melting peak temperature (T_m), melting enthalpy (ΔH_m), and PVDF-normalized degree of crystallinity (X_c). The addition of ENR-50 strongly influenced the crystallization behavior of PVDF, whereas the melting transition was affected to a lesser extent. The crystallization temperature (T_c) of neat PVDF is 135.8 °C (Table 1). Upon incorporating 20–60 wt% ENR-50, T_c shifts to higher values of 138.5–139.3 °C, with a maximum of 139.3 °C for the 50/50 PVDF/ENR-50 blend. At the same cooling rate, higher T_c values indicate that PVDF crystallizes more readily during cooling, requiring a smaller temperature drop below its melting temperature. This behavior may be consistent with facilitated heterogeneous nucleation at the

PVDF/ENR-50 interfaces due to enhanced interfacial interactions between the two phases, as illustrated in Figure 2. Therefore, the increase in Tc at low-to-intermediate ENR-50 contents may be attributed to heterogeneous nucleation of PVDF at the PVDF/ENR-50 interfaces. As indicated by the morphologies in Figures 1(a–d), increasing the ENR-50 content initially produces finer, more closely spaced, and more interconnected ENR-50 domains, thereby increasing the interfacial area available for nucleation. Intermolecular interactions between the polar oxirane groups of ENR-50 and the dipolar C–F groups of PVDF may also modify the interfacial free-energy barrier for the formation of stable PVDF nuclei (Figure 2). In polymer blends, it has been established that interfaces and dispersed domains can reduce the free-energy barrier to nucleation, thereby shifting the crystallization peak toward higher temperatures [54, 55]. Furthermore, the temperature difference between the melting and crystallization temperatures, estimated as $T_m - T_c$, decreased from 32.6 °C for neat PVDF to 29.2, 29.0, 28.9, and 27.7 °C for the PVDF/ENR-50 80/20, 70/30, 60/40, and 50/50 blends, respectively. The minimum value (27.7 °C) observed for the 50/50 blend further indicates that PVDF crystallization occurred most readily near the apparent co-continuous composition. At this composition, the extensive PVDF/ENR-50 interfacial area may provide a relatively large number of heterogeneous nucleation sites, while the PVDF phase remains sufficiently interconnected to permit chain transport and crystal growth.

In Figure 5 and Table 1, the *FWHM* of the PVDF crystallization exotherm decreased from 5.7 °C for neat PVDF to a minimum of 4.2 °C for the 60/40 PVDF/ENR-50 blend, while the PVDF-normalized crystallinity (X_c) increased from 50.3% to a maximum of 54.2%. The concurrence of the minimum FWHM and maximum X_c suggests that the apparently co-continuous morphology provided numerous, relatively uniformly distributed interfacial nucleation sites, allowing PVDF to crystallize within a narrower temperature interval and form a slightly higher final crystalline fraction. However, the maximum T_c occurred for the 50/50

rather than the 60/40 PVDF/ENR-50 blend, indicating that crystallization at a higher temperature during cooling does not necessarily lead to the highest final degree of crystallinity. This is because Tc, the FWHM of the crystallization exotherm, and X_c describe different aspects of the non-isothermal crystallization process [56]. Specifically, T_c indicates the temperature at which the crystallization rate reaches its maximum, FWHM reflects the temperature interval over which most crystallization occurs, and X_c represents the final amount of crystalline PVDF formed. These parameters are collectively influenced by the competing effects of crystal nucleation and growth, PVDF chain mobility and transport, and spatial confinement within the blend morphology [57, 58]. At ENR-50 contents above 50 wt%, the progressive broadening of the crystallization peak and the overall decrease in X_c, which reached 43.7% for the 20/80 blend, are consistent with the increasingly isolated and spatially confined PVDF domains observed in Figure 1. Although the increased interfacial area may still promote nucleation, the loss of PVDF phase continuity restricts chain transport and subsequent lamellar growth.

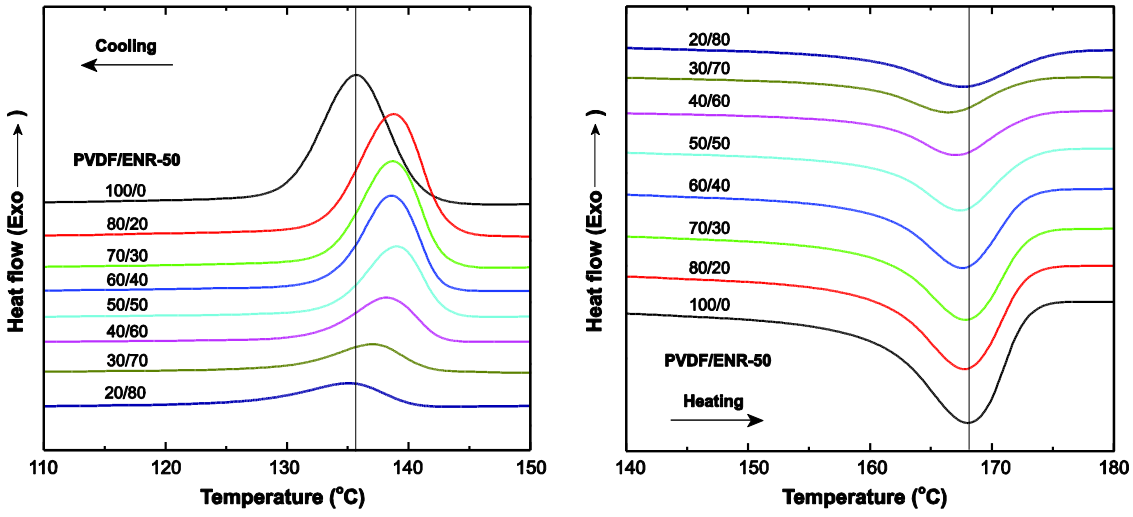


Figure 5. DSC thermograms obtained during cooling (left) and heating (right) for PVDF/ENR-50 blends with various compositions.

Table 1. Crystallization temperature (T_c), full width at half maximum of the crystallization peak (FWHM), melting temperature (T_m), melting enthalpy (ΔH_m), and degree of crystallinity (X_c) of PVDF in PVDF/ENR-50 blends.

Materials	T_c (°C)	**FWHM (°C)**	T_m (°C)	ΔH_m (J/g)	X_c (%)
Neat PVDF	135.8	5.7	168.4	52.6	50.3
PVDF/ENR-50 = 80/20	139.1	5.1	168.3	44.8	53.6
PVDF/ENR-50 = 70/30	139.0	4.7	168.0	39.5	54.0
PVDF/ENR-50 = 60/40	138.9	4.2	167.8	34.0	54.2
PVDF/ENR-50 = 50/50	139.3	4.6	167.0	27.2	52.1
PVDF/ENR-50 = 40/60	138.5	5.2	167.0	19.7	47.1
PVDF/ENR-50 = 30/70	137.2	6.3	166.4	16.2	51.6
PVDF/ENR-50 = 20/80	135.3	7.5	166.4	9.1	43.7

3.14 Dynamic mechanical analysis (DMA)

Figure 6 shows the storage modulus (E′) and loss tangent (tan δ) as functions of temperature for neat PVDF (PVDF/ENR-50 = 100/0) and PVDF/ENR-50 blends with various blend ratios, measured at a fixed frequency of 1 Hz. Neat PVDF exhibits the highest storage modulus over most of the investigated temperature range. Its storage modulus decreases gradually with increasing temperature and shows only a comparatively small reduction around the principal amorphous-phase relaxation, or glass-transition region, of PVDF. This limited modulus reduction is attributed to the semicrystalline structure of PVDF, in which the crystalline regions remain mechanically effective above the glass transition of the amorphous phase and act as physical crosslinks that restrict segmental motion and maintain mechanical stiffness [59, 60]. The principal relaxation of the amorphous PVDF phase is commonly observed at approximately -35 to -41 °C [61, 62] and is often designated as the β-relaxation or α_a-relaxation, depending on the nomenclature adopted [59], as indicated in the inset of Figure

6. This relaxation is associated with cooperative segmental motion in the amorphous regions of PVDF and is generally identified as the dynamic glass transition of PVDF, distinguishing it from higher-temperature relaxations associated with molecular motions involving the crystalline regions [63]. As the ENR-50 content increased, E′ decreased progressively, and the modulus drop in the ENR-50 glass-transition region became increasingly pronounced. This behavior primarily results from replacing the stiff, semicrystalline PVDF phase with the softer, predominantly amorphous ENR-50 phase. In addition, the increasing content and connectivity of ENR-50 enhanced segmental mobility and reduced the ability of the blends to store elastic energy. This trend agrees with the mechanical properties shown in Figures 3 and 4: increasing ENR-50 content reduced the initial slope of the stress–strain curves, Shore A hardness, and tension set, while increasing extensibility. This behavior is also consistent with the SEM morphologies shown in Figure 1. The relatively high modulus of the PVDF-rich blends originates from the continuous PVDF matrix, whereas the marked decrease in modulus at intermediate compositions accompanies the formation of interconnected ENR-50 domains and the progressive loss of PVDF continuity.

After the principal glass transition, the storage modulus continued to decrease with increasing temperature, although the extent of this decrease depended strongly on the blend composition. The PVDF-rich blends retained comparatively high modulus values because the continuous semicrystalline PVDF phase provided a persistent load-bearing structure. In contrast, the ENR-50-rich blends exhibited much lower E', particularly above the glass transition of ENR-50, because the uncrosslinked ENR-50 matrix entered a highly mobile rubbery state and the PVDF phase no longer formed a continuous reinforcing network. This result is consistent with the very high elongation at break and relatively low tensile stress of the ENR-50-rich blends shown in Figure 3.

In Figure 6, two principal tan δ relaxation peaks can be clearly observed: one at

approximately −36 °C and another near −9 °C. The lower-temperature relaxation is assigned to the amorphous-phase relaxation of PVDF, whereas the higher-temperature peak corresponds to the glass transition of ENR-50. The persistence of two distinguishable relaxation peaks indicates that the blends remain phase-separated over the investigated composition range. However, the composition-dependent shifts of these peaks from the corresponding neat-component values suggest that the two phases are not completely independent and that limited interfacial mixing or partial compatibility may occur. The intensity of the PVDF relaxation decreased progressively with decreasing PVDF content, whereas the ENR-50 relaxation became more pronounced as the ENR-50 content increased. These changes primarily reflect the changing relative proportions of the two relaxing phases. The exceptionally intense tan δ peak of ENR-50 also indicates substantial mechanical-energy dissipation associated with cooperative segmental motion of the rubber phase. Thus, increasing the ENR-50 content transforms the blends from relatively stiff, low-damping materials into softer materials with greater damping capability. This is supported by the DSC results (Figure 5 and Table 1). At low-to-intermediate ENR-50 contents, the PVDF-normalized degree of crystallinity (X_c) remained approximately 52–54%, and the crystalline PVDF regions continued to reinforce the amorphous phase. However, when ENR-50 became the major continuous phase, E' decreased markedly, even though the PVDF crystallinity did not decrease monotonically. Therefore, the DMA modulus is governed not only by the degree of PVDF crystallinity but also, and more importantly, by the absolute PVDF fraction, phase continuity, the temperature relative to the two glass transitions, and the ability of the crystalline PVDF phase to form a continuous stress-bearing pathway [63]. The glass-transition temperature of a completely miscible binary blend is frequently approximated using the Fox equation [64]:

$$\frac{1}{T_g} = \frac{W_1}{T_{g1}} + \frac{W_2}{T_{g2}} \tag{2}$$

where W_1 and W_2 are the weight fractions of the two components, T_{g1} and T_{g2} are their respective glass-transition temperatures, and all temperatures are expressed in kelvin.

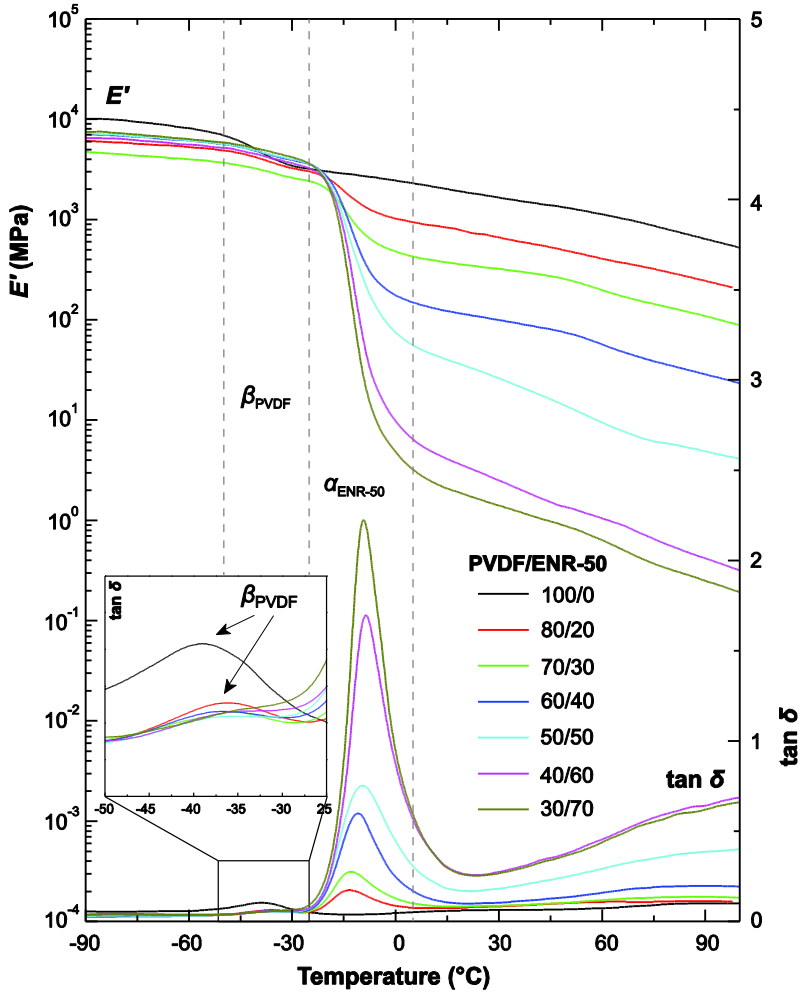


Figure 6. Storage modulus (E') and loss tangent ($\tan\delta$) as functions of temperature for neat PVDF and PVDF/ENR-50 blends with various blend ratios, measured at a frequency of 1 Hz.

Equation (2), the Fox equation, predicts a single composition-dependent T_g for an ideally miscible blend. It should therefore be used here as a reference for complete miscibility rather than as a direct prediction of the two separate relaxation temperatures observed experimentally. Figure 7 compares the glass-transition relaxation temperatures assigned to the PVDF-rich and ENR-50-rich phases with the single-T_g values predicted by the Fox equation. The blends clearly retained two composition-dependent relaxation temperatures rather than

exhibiting the single T_g predicted for a completely miscible blend. This behavior confirms a phase-separated system with partial compatibility in the nonvulcanized PVDF/ENR-50 blends. In Figure 7, it is clear that the ENR-50 relaxation shifts markedly to higher temperatures as the PVDF content increases, whereas the PVDF relaxation shows a smaller displacement. These shifts suggest restricted segmental mobility caused by limited chain interpenetration, entanglement, and possible polar interactions between the oxirane groups of ENR-50 and the dipolar (CH2–CF2) units of PVDF at the interface (Figure 2). The upward shift of the ENR-50 relaxation in PVDF-rich blends indicates that ENR-50 chain mobility was constrained by the stiff PVDF matrix and interfacial interactions. As the ENR-50 phase became increasingly interconnected, this constraint decreased and its relaxation approached that of neat ENR-50. The PVDF relaxation may also have been influenced by crystalline-phase constraints, interfacial interactions, phase dimensions, and confinement. However, because X_c varied non-monotonically with composition, the relaxation shifts cannot be attributed solely to crystallinity. DMA therefore supports partial interfacial interaction but cannot independently determine the precise molecular interactions or interfacial-layer thickness.

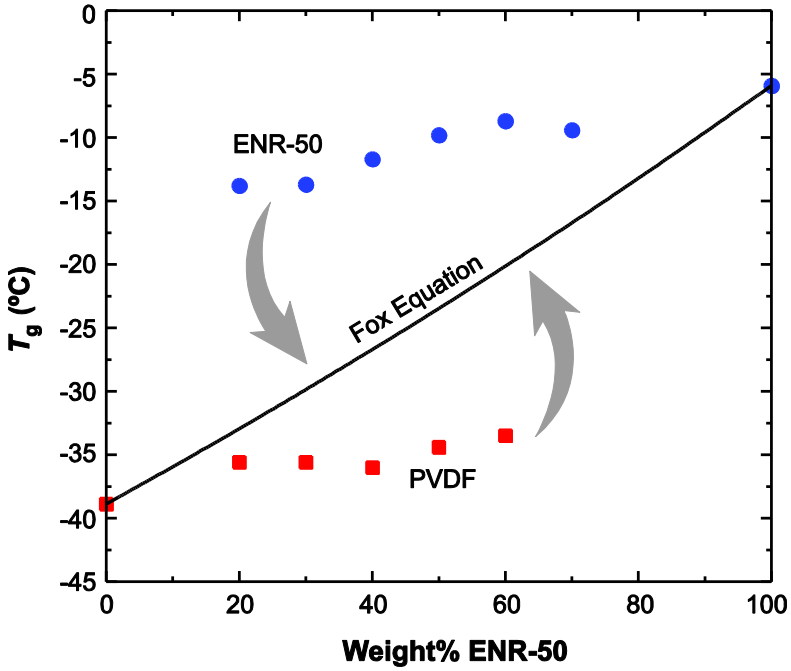


Figure 7. Relaxation temperatures assigned to the PVDF-rich and ENR-50-rich phases as functions of ENR-50 content in PVDF/ENR-50 blends. The solid line represents the single glass-transition temperature predicted by the Fox equation for a completely miscible blend.

Figure 8 shows the storage modulus (E') and loss factor (tan δ), measured at −10 and 25 °C, as functions of ENR-50 content. The composition dependence of both modulus and damping corresponds closely to the morphological evolution observed by SEM in Figure 1 (also shown above these plots for close comparison). The results can be divided qualitatively into three compositional regions: a PVDF-continuous region, an apparently co-continuous transition region, and an ENR-50-continuous region. In the first region, containing less than approximately 40 wt% ENR-50, the ENR-50 exists primarily as dispersed or partially interconnected domains within the continuous PVDF matrix. The storage modulus decreases progressively with increasing ENR-50 content, whereas tan δ increases only moderately. The continuous PVDF matrix continues to control the dynamic stiffness, while the increasing amount of ENR-50 provides a progressively larger dissipative contribution. This interpretation agrees with the comparatively high hardness and tensile stress of the 80/20 and 70/30 blends and with their limited deformation at break in Figures 3 and 4. In the intermediate region, at approximately 40–60 wt% ENR-50, the morphology changes from a PVDF-continuous structure to an apparently co-continuous structure and then approaches the second phase-inversion boundary. According to Figure 1, the principal apparent co-continuous compositions are 60/40 and 50/50 PVDF/ENR-50, whereas the 40/60 blend lies close to the transition toward an ENR-50-continuous morphology. Within this region, E' decreases sharply, while tan δ at both −10 and 25 °C increases substantially. The sharp changes arise because both phases become sufficiently interconnected to influence the macroscopic response. The diminishing PVDF network reduces dynamic stiffness, whereas the growing continuous ENR-50 pathways increase segmental mobility and mechanical energy dissipation. The transition is therefore not caused by blend composition alone but by the accompanying change in phase connectivity.

This result is consistent with the marked decrease in hardness and tensile stress and the increase in elongation and elastic recovery (Figures 3 and 4) observed near the co-continuous and phase-inversion compositions. The effect is particularly pronounced for tan δ at −10 °C because this temperature is close to the ENR-50 relaxation peak. Consequently, ENR-50-rich compositions dissipate considerably more mechanical energy at −10 °C than at 25 °C. At 25 °C, both phases are above their principal amorphous-phase relaxations, but the increasing continuity of the soft ENR-50 phase still produces a clear increase in damping. At ENR-50 contents above approximately 60 wt%, ENR-50 forms the principal continuous matrix and PVDF is present mainly as dispersed domains. The modulus therefore approaches a low value controlled predominantly by the soft, uncrosslinked ENR-50 phase. The comparatively small subsequent change in E' indicates that further reduction of an already discontinuous PVDF phase has a less pronounced effect than the initial loss of PVDF continuity. Similarly, the tendency of tan δ to level off at high ENR-50 contents indicates that damping is increasingly governed by the continuous ENR-50 matrix. Therefore, the DMA results corroborate the SEM, tensile, hardness, tension-set, and DSC findings. The PVDF-rich blends exhibit high stiffness because of their continuous semicrystalline PVDF structure, whereas the apparently co-continuous region shows a rapid transition from stiffness-dominated to damping-dominated behavior. In contrast, the ENR-50-rich blends exhibit low modulus, high extensibility, and enhanced energy dissipation because the rubber phase forms the continuous matrix. Among the investigated blends, the intermediate compositions therefore provide the most adjustable balance between dynamic stiffness and damping, whereas the ENR-50-rich compositions may be more suitable for flexible or vibration-damping applications.

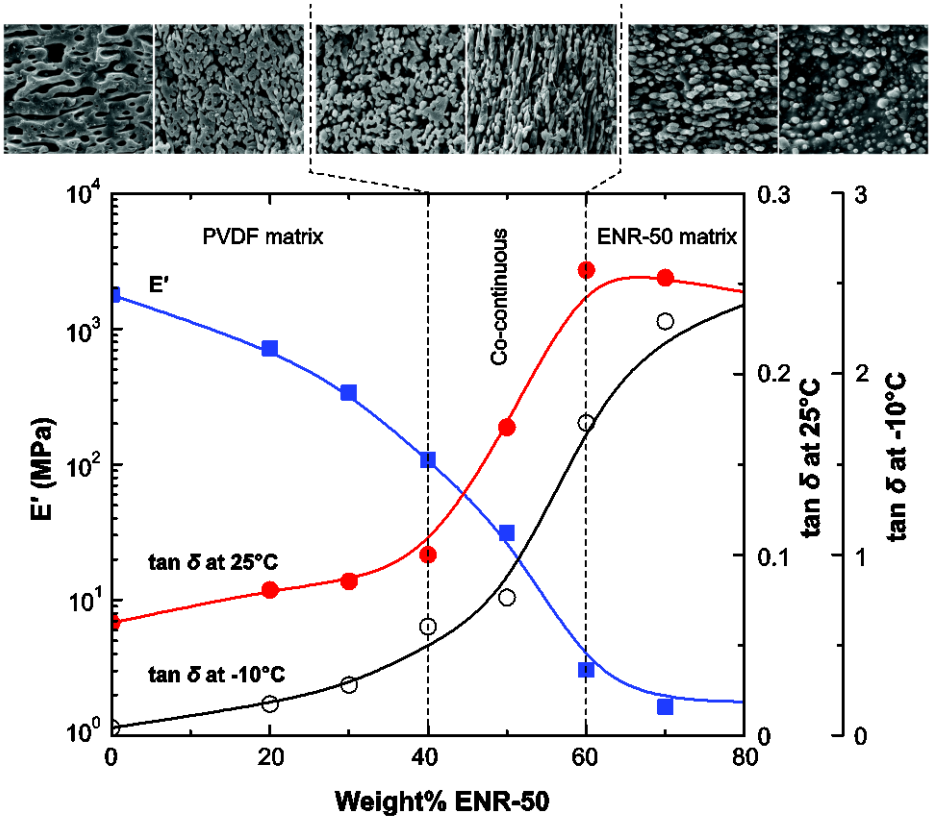


Figure 8. Storage modulus (E') and loss tangent ($\tan\delta$) measured at -10 and 25°C as functions of ENR-50 content in PVDF/ENR-50 blends. The corresponding phase morphologies identified from the SEM micrographs in Figure 1 are indicated above the graph.

3.2 Effect of barium titanate (BT) particles on PVDF/ENR-50 blends

3.2.1 Morphological properties

Barium titanate (BT) is a ferroelectric ceramic with very high dielectric permittivity; therefore, its incorporation into PVDF-based materials is a practical approach to increasing dielectric polarization and developing flexible high-permittivity composites. In a multiphase PVDF/ENR-50 blend, the benefit of BT depends not only on its intrinsic dielectric response but also on its dispersion and selective localization, because confinement of the particles within one polymer phase can concentrate the functional filler and modify both the phase morphology and the resulting electrical and mechanical properties. Figure 9 shows SEM micrographs of the 80/20 and 50/50 PVDF/ENR-50 nonvulcanized blends containing 5 vol% BT. These two

PVDF/ENR-50 blend ratios (i.e., 80/20 and 50/50) were selected for BT incorporation because they represent two distinctly different morphological states. The 80/20 blend exhibits a PVDF-continuous/ENR-50-dispersed morphology, whereas the 50/50 blend lies within the main apparent co-continuous region. Therefore, comparing these two compositions allows the effect of BT localization to be evaluated in both a PVDF-rich matrix–droplet structure and a morphology close to phase inversion, where relatively small rheological changes may strongly alter phase continuity. The BT-filled PVDF/ENR-50 blends were examined on unetched cryo-fractured surfaces. SEM images in Figure 9 indicate that the comparatively rough regions are mainly assigned to semicrystalline PVDF, whereas the smoother regions are associated with the soft, predominantly amorphous ENR-50 phase. Furthermore, the bright particles observed predominantly in the smoother regions indicate preferential localization of BT particles in the ENR-50 phase in both blend compositions. Specifically, it is observed that the overall PVDF-continuous/ENR-50-dispersed morphology is retained after BT addition in the 80/20 PVDF/ENR-50 blend in Figure 9(a), consistent with the unfilled blend shown in Figure 1(a). However, the average ENR-50 domain size increased from approximately 6.5 μm in the unfilled blend to approximately 11.4 μm in the BT-filled blend. This coarsening indicates that BT did not behave solely as an interfacial compatibilizer. Instead, its preferential incorporation into ENR-50 altered the effective rheology of the dispersed rubber phase. The resulting increase in the viscosity and resistance to deformation of the particle-loaded ENR-50 domains would reduce their breakup under the imposed shear field, thereby producing larger dispersed domains. Therefore, particle localization may be governed by a combination of thermodynamic wetting preference and kinetic trapping during melt mixing; thus, the lower viscosity of ENR-50 alone should not be considered definitive evidence of the equilibrium location of BT. Previous studies on particle-filled immiscible blends have similarly shown that particles

localized within one phase can change the viscosity ratio, retard droplet deformation and breakup, and consequently alter the final domain size and phase continuity [65, 66].

In Figure 9(B), a more pronounced morphological change is observed for the 50/50 blend. The unfilled 50/50 PVDF/ENR-50 blend exhibits an apparently co-continuous morphology, as shown in Figure 1(d). However, the BT-filled blend mainly shows PVDF-rich droplets dispersed within a continuous ENR-50-rich matrix. Thus, BT addition may influence the phase-inversion behavior and suppress the apparent co-continuous structure at this composition. This change can be attributed to the preferential loading of BT into ENR-50, which substantially increased the effective viscosity and elasticity of that phase and altered the ENR-50/PVDF viscosity ratio. It has been recognized that phase continuity in melt-mixed immiscible polymer blends is governed by blend composition, viscosity and elasticity ratios, interfacial tension, and the dynamic balance among domain deformation, breakup, and coalescence [49, 67]. Therefore, the incorporation of BT particles may modify the rheological balance between the PVDF and ENR-50 phases. This modification may suppress phase breakup or coalescence and favor greater continuity of the ENR-50 phase rather than co-continuity of both phases. Furthermore, the 5 vol% BT loading corresponds to approximately 18–20 wt% relative to the polymer, depending on the densities used, and is therefore sufficiently high to cause a substantial rheological perturbation. This interpretation agrees with previous studies showing that selectively localized particles can shift phase inversion, enlarge dispersed domains, or transform co-continuous morphologies into matrix–droplet structures when the filler loading strongly changes the rheology of one phase [65]. Therefore, BT acts both as a functional dielectric filler and as a morphology-controlling component in the PVDF/ENR-50 blends. Its preferential localization in the ENR-50 phase preserves the PVDF-matrix/ENR-50-dispersed morphology of the 80/20 blend but induces substantial morphological restructuring in the 50/50 blend. These morphological changes should be taken

into account when interpreting the subsequent mechanical, thermal, dynamic mechanical, and dielectric properties.

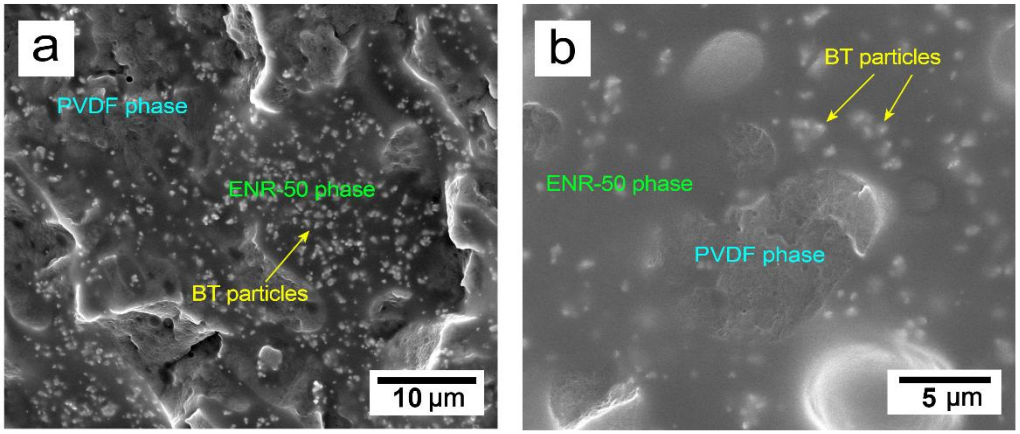


Figure 9. SEM micrographs of nonvulcanized PVDF/ENR-50 blends containing 5 vol% BT: (a) 80/20 and (b) 50/50 blend ratios.

3.2.2 Mechanical properties

Figure 10 shows the stress–strain curves of the 80/20 and 50/50 PVDF/ENR-50 non-vulcanized blends with and without 5 vol% BT particles. The mechanical effect of BT should be considered together with its preferential localization in the ENR-50 phase and the associated morphological changes shown in Figure 9. Thus, BT does not necessarily act as a conventional reinforcing filler uniformly distributed throughout the entire blend; instead, its contribution depends strongly on whether the BT-containing ENR-50 phase is dispersed or continuous. In Figures 3 and 10, it is observed that the unfilled 80/20 PVDF/ENR-50 blend exhibits the highest initial slope and tensile stress but relatively low deformation at break. This response is characteristic of plastic-like behavior, as previously discussed in Figure 3, and is associated with the continuous semicrystalline PVDF matrix rather than simply with brittle PVDF. With this type of morphology, the PVDF phase provides the principal stress-bearing pathway, whereas ENR-50 is present as a dispersed soft phase, as shown in Figure 1(a). In contrast, in

the BT-filled, nonvulcanized 80/20 PVDF/ENR-50 blend, incorporation of BT did not significantly affect the stress–strain curve or tensile properties (Figure 10). This indicates that, although BT was preferentially localized in the ENR-50 phase dispersed within the PVDF matrix, the tensile behavior was still dominated by the continuous PVDF phase. This result is consistent with the SEM observations in Figures 1(a) and 9(a), which show that BT incorporation did not alter the principal PVDF-continuous/ENR-50-dispersed morphology. It is also anticipated that the BT-containing ENR-50 domains remained discontinuous in the 80/20 blend and therefore could not establish a continuous rigid particle network capable of governing macroscopic stress transfer. Consequently, any local stiffening of the ENR-50 domains by BT was comparatively small relative to the dominant contribution of the continuous semicrystalline PVDF matrix. Moreover, the similarity between the two 80/20 stress–strain curves in Figure 9 indicates that the larger, more breakup-resistant ENR-50 domains did not cause a marked deterioration in the tensile response. This suggests that the PVDF matrix remained sufficiently continuous and that interfacial defects or BT agglomerates were not severe enough to dominate failure under the investigated conditions. Nevertheless, the absence of a pronounced improvement also indicates that the BT particles did not provide effective direct reinforcement of the continuous PVDF phase because they were localized mainly within the dispersed ENR-50 domains.

By contrast, in Figures 3 and 9, the 50/50 unfilled PVDF/ENR-50 simple blend showed uniform deformation with low modulus and high elongation at break, indicating more pronounced elastomer-like behavior. This is attributed to the soft ENR-50 phase in the blend, which provides low modulus and stress at break but high flexibility with an apparently co-continuous morphology, as discussed in Figure 1(d). In this case, the interconnected PVDF phase provides stiffness and facilitates stress transfer, whereas the interconnected ENR-50 phase accommodates extensive deformation and enhances the elasticity of the blend.

Therefore, its mechanical response reflects the combined contributions of both phases rather than the effect of ENR-50 alone.

However, in Figure 9, the BT-filled 50/50 PVDF/ENR-50 simple blend showed a pronounced decrease in tensile stress together with a substantial increase in deformation at break, to approximately 800% compared with about 420% in the unfilled blend. This behavior is attributed to the different phase morphology of the 50/50 PVDF/ENR-50 blend. The unfilled, nonvulcanized 50/50 PVDF/ENR-50 blend exhibits an apparently co-continuous morphology, as shown in Figure 1(d), in which both PVDF and ENR-50 form interconnected pathways. In contrast, incorporation of 5 vol% BT transformed the blend morphology into PVDF domains dispersed within a continuous ENR-50 matrix, as indicated in Figure 9(b). This morphological change reduces the continuity of the stiff PVDF stress-bearing network and increases the contribution of the soft ENR-50 phase, resulting in lower tensile stress but greater deformation at break, as shown in Figure 10. The reduction in tensile stress is therefore attributed primarily to the loss of a continuous PVDF stress-bearing pathway. In the unfilled 50/50 blend, the continuous or highly interconnected PVDF phase can transfer stress throughout the specimen. Following BT addition, preferential particle localization in ENR-50 alters the rheological balance and promotes continuity of the soft ENR-50-rich phase, while PVDF becomes more dispersed. The mechanical response consequently becomes governed mainly by the soft, uncrosslinked ENR-50 matrix, producing lower stiffness and tensile stress but allowing considerably greater deformation before failure. Although rigid ceramic particles commonly increase the modulus of polymer composites when they are well dispersed and adequately bonded to a continuous polymer matrix [68], this conventional reinforcement effect does not appear to dominate the mechanical behavior of the present PVDF/ENR-50 blends. Instead, the observed changes in mechanical properties seem to be governed more strongly by BT-induced morphological restructuring associated with the preferential localization of BT in the ENR-50

phase [69]. Moreover, the particles are concentrated mainly in the ENR-50 phase rather than uniformly reinforcing the PVDF phase. The reduction in tensile stress should therefore not be interpreted automatically as evidence of poor BT reinforcement alone; it reflects the combined effects of particle localization, loss of PVDF continuity, possible particle agglomeration, altered interfacial stress transfer, and the non-vulcanized nature of the continuous ENR-50 phase. Moreover, the increased deformation at break of the BT-filled 50/50 blend is noteworthy because rigid ceramic fillers often reduce extensibility when their addition does not change the matrix morphology. In the present system, however, the BT-induced transformation from an apparently co-continuous structure to an ENR-50-continuous/PVDF-dispersed structure increases the contribution of the deformable rubber phase. Thus, the morphology effect outweighs the usual strain-restricting effect of the ceramic particles. Similar studies of particle-filled immiscible polymer blends have shown that selective filler localization can alter phase inversion and phase continuity, producing mechanical-property changes that cannot be explained by conventional composite reinforcement alone [65, 70]. This interpretation is also consistent with previous work on dynamically cured PVDF/ENR-50/BT composites, in which the distribution of BT and the phase morphology strongly influenced the resulting mechanical and functional properties [66]. However, the present blends are non-vulcanized; therefore, the continuous ENR-50 phase has no permanent chemical network. Its large deformation is supported mainly by chain entanglements, physical interactions, and constraints imposed by the dispersed PVDF domains. Consequently, the BT-filled 50/50 blend provides greater flexibility but lower load-bearing capability than its unfilled, apparently co-continuous counterpart.

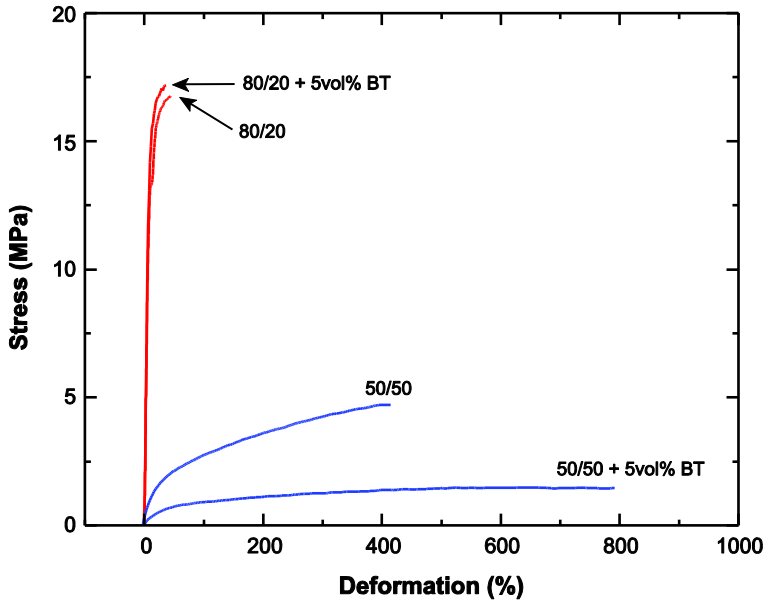


Figure 10. Stress–strain curves of the 80/20 and 50/50 PVDF/ENR-50 nonvulcanized blends with and without 5 vol% BT particles.

3.2.3 Dynamic mechanical analysis (DMA)

Figure 11 shows the temperature dependence of the storage modulus (E') and loss tangent (tan δ) for the 80/20 and 50/50 PVDF/ENR-50 non-vulcanized blends with and without 5 vol% BT, measured at 1 Hz. The storage modulus represents the elastic or energy-storage component of the dynamic response, whereas tan δ represents the ratio of viscous energy dissipation to elastic energy storage. Figure 11(a) shows that the 80/20 blends exhibit relatively high E' values over the investigated temperature range, consistent with the continuous semicrystalline PVDF matrix identified in Figures 1(a) and 9(a). This result agrees with the previous composition-dependent DMA results in Figure 6, where PVDF-rich blends retained high dynamic stiffness because the PVDF crystalline regions acted as persistent physical constraints above the amorphous-phase relaxation. Furthermore, the BT-filled 80/20 blend exhibits a moderately higher E' than the unfilled blend over much of the temperature range, indicating a limited dynamic-reinforcement effect arising from the high rigidity of BT and the reduced deformability of the BT-containing ENR-50 domains. Even though BT is

preferentially localized in the dispersed ENR-50 phase, the particles can restrict local rubber-chain motion and increase the effective stiffness of those domains. Stress may also be transferred from the continuous PVDF matrix through the PVDF/ENR-50 interface to the particle-containing ENR-50 domains. However, the increase is comparatively moderate because the BT-rich ENR-50 phase remains discontinuous and therefore does not form a continuous reinforcing network. Moreover, both the filled and unfilled 80/20 blends retain the two principal relaxation regions previously identified in Figure 6: a lower-temperature relaxation associated mainly with the amorphous PVDF phase and a higher-temperature relaxation associated with the glass transition of ENR-50 component. The persistence of these relaxations after BT addition indicates that BT does not make PVDF and ENR-50 completely miscible. The ENR-50-related tan δ peak becomes more pronounced in the presence of BT, while its position appears to change only slightly. The increase in peak intensity may arise from enhanced interfacial friction and greater mechanical-energy dissipation at the ENR-50/BT and PVDF/ENR-50 interfaces. Nevertheless, an increased tan δ peak should not be interpreted solely as stronger molecular interaction. Because tan δ is the ratio E″/E′, its magnitude can change through variations in either the loss modulus or the storage modulus. Therefore, the enhanced ENR-50 peak provides evidence of modified relaxation and dissipation behavior but does not independently prove chemical bonding between BT and ENR-50.

Figure 11(b) shows a much larger decrease in E' through the ENR-50 relaxation region than that observed for the 80/20 blend. This behavior is consistent with the higher ENR-50 content and the greater contribution of the soft rubber phase. The previous DMA results in Figures 6 and 8 showed that the storage modulus decreased sharply near the apparently co-continuous and phase-inversion region because the growing ENR-50 pathways increased segmental mobility while the PVDF stress-bearing network progressively lost continuity. Below the ENR-50 glass-transition region, the BT-filled 50/50 blend exhibits a slightly higher

E' than the corresponding unfilled blend. At these low temperatures, the ENR-50 phase is in a glassy or transition state, and the rigid BT particles further restrict local chain mobility, so the intrinsic filler-stiffening effect remains observable. Above the ENR-50 relaxation, however, the E' of the BT-filled blend decreases more strongly and becomes lower than that of the unfilled blend. This apparent reversal indicates that phase morphology, rather than ceramic rigidity alone, controls the high-temperature dynamic response. The unfilled 50/50 blend is anticipated to exhibit an apparently co-continuous morphology, as shown in Figure 1(a), allowing the interconnected semicrystalline PVDF phase to maintain a continuous dynamic load-bearing pathway after the ENR-50 phase enters its rubbery state. In contrast, the BT-filled 50/50 blend exhibits a continuous ENR-50 phase with dispersed PVDF, as shown in Figure 9(a). Once the ENR-50 matrix passes through its glass transition, its segmental mobility increases markedly, and the discontinuous PVDF domains can no longer sustain the same macroscopic stiffness as the PVDF network in the unfilled blend. Consequently, the morphology-induced loss of PVDF continuity outweighs the local stiffening contribution of BT. This behavior is consistent with the tensile results in Figure 10: the BT-filled 50/50 blend exhibits lower tensile stress and substantially greater deformation because its mechanical and dynamic responses are dominated by the continuous, soft ENR-50 matrix. Thus, the tensile and DMA results provide mutually supporting evidence that BT addition changed not only the local stiffness of the material but also the connectivity of its constituent phases. The ENR-50-related tan δ peak of the BT-filled 50/50 blend is substantially higher than that of the unfilled blend. This indicates enhanced mechanical energy dissipation during segmental relaxation of the ENR-50-rich phase. Several effects may contribute concurrently: increased continuity of ENR-50, friction or constrained motion near the BT/ENR-50 interfaces, heterogeneity of the particle-containing rubber phase, and stress transfer between the soft matrix and the dispersed PVDF domains. The higher tan δ values above the main relaxation also indicate that the BT-filled

material remains more dissipative in the rubbery region. The peak position appears to change much less than its intensity. Therefore, the principal effect of BT is more clearly expressed through changes in stiffness, phase connectivity, and damping magnitude than through a major displacement of the ENR-50 glass-transition temperature. Therefore, the effect of BT is composition-dependent. In the 80/20 blend, the continuous PVDF matrix is preserved, and BT produces a moderate increase in dynamic stiffness without substantially changing the tensile response. In the 50/50 blend, BT changes the morphology from apparently co-continuous to ENR-50-continuous/PVDF-dispersed. This change reduces tensile strength and rubbery-state storage modulus but increases deformation at break and damping. Thus, BT serves not only as a high-permittivity functional filler but also as a morphology-controlling additive that adjusts the balance among stiffness, flexibility, and energy dissipation.

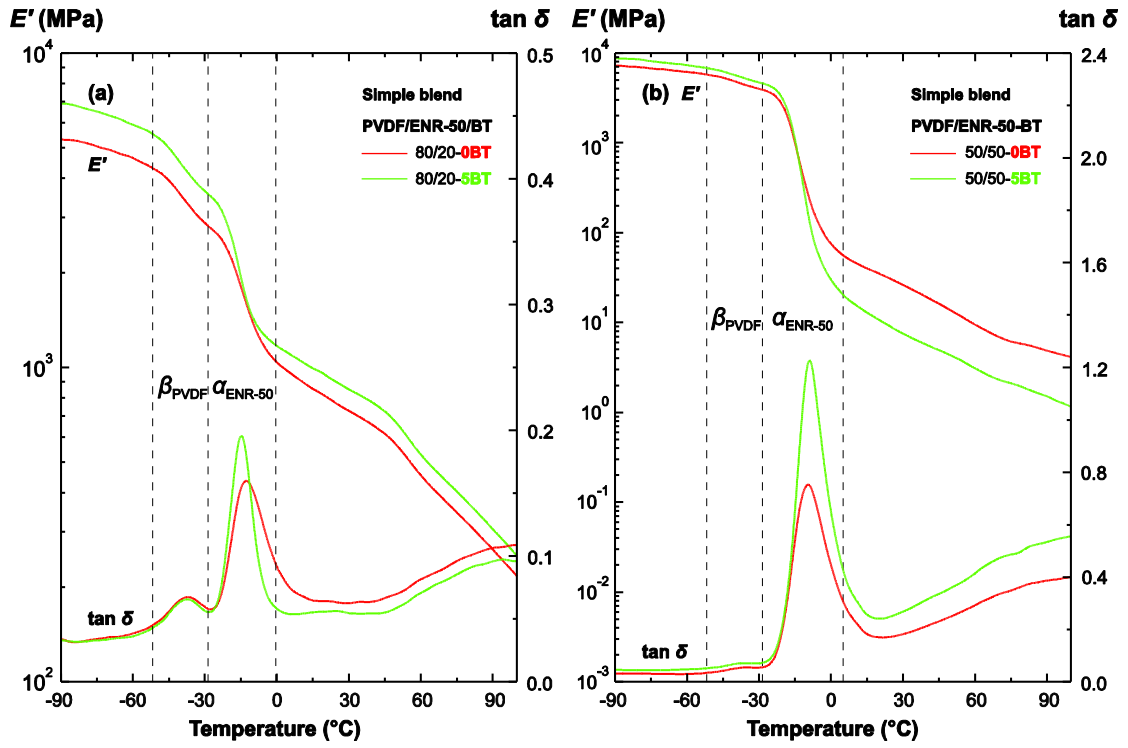


Figure 11. Temperature dependence of the storage modulus (E′) and loss tangent (tan δ) for (a) 80/20 and (b) 50/50 PVDF/ENR-50 non-vulcanized blends without and with 5 vol% BT, measured at 1 Hz.

3.2.4 Dielectric properties

Dielectric properties of the 80/20 and 50/50 PVDF/ENR-50 non-vulcanized blends with and without 5 vol% BT filler are shown in Figure 12. Figure 12(a) presents the real part of the dielectric permittivity (ε′), whereas Figure 12(b) presents the dielectric loss (ε″) as functions of frequency at room temperature. The dielectric permittivity (ε′) of all materials is frequency-dependent and decreases with increasing frequency. In Figure 12(a), the dielectric permittivity (ε′) of all blends is frequency-dependent and decreases with increasing frequency because dipole orientation cannot follow the rapid high-frequency alternation of the electric field [70]. At low frequencies, dipolar, interfacial, and space-charge polarization processes have sufficient time to respond to the applied field and therefore make substantial contributions to ε′. As the frequency increases, the slower polarization mechanisms can no longer follow the rapid field reversal, resulting in the observed decrease in permittivity [71, 72]. At a given frequency, neat PVDF exhibits a higher dielectric permittivity than neat ENR-50 because of the strong dipole moments associated with the CF_2 groups in PVDF. This difference is clearly shown in Figure 12(a), where neat PVDF exhibits ε′ values of approximately 10–11 at low frequency, compared with approximately 8–9 for neat ENR-50. The higher permittivity of PVDF over the investigated frequency range is primarily attributed to these strong dipole moments. As the frequency increases, the slower segmental and space-charge polarization processes contribute progressively less to the permittivity of both polymers. Interestingly, the PVDF/ENR-50 blends exhibit higher dielectric permittivity than either neat PVDF or neat ENR-50. This enhancement is attributed to Maxwell–Wagner–Sillars interfacial polarization, arising from the accumulation of charge carriers at the interfaces between the PVDF and ENR-50 phases because of their different electrical conductivities and dielectric permittivities [66, 73].

Moreover, incorporating BT into the blends significantly increases permittivity. Adding a ceramic filler with high dielectric permittivity, such as BT (ε′ ≈ 2000 to 3500) [74], to polymer

phases with relatively low dielectric permittivity ($\varepsilon' \approx 2–10$) [75] is expected to have this effect. The enhanced dielectric permittivity of BT-filled PVDF/ENR-50 composites may also result from the different conductivities and permittivities of the three phases in the composite (PVDF, ENR, and BT), which enable interfacial polarization [49, 65, 66]. Furthermore, the BT-filled PVDF/ENR-50 composite with high PVDF content (80/20 PVDF/ENR-50) shows a higher dielectric constant than the BT-filled 50/50 PVDF/ENR-50 composite with lower PVDF content because of the high dielectric permittivity of PVDF.

Figure 12(b) shows the dielectric loss (ε'') versus frequency for the 80/20 and 50/50 PVDF/ENR-50 nonvulcanized blends with and without BT filler. Neat PVDF exhibits two relaxation peaks, at low and high frequencies, corresponding to relaxations in the crystalline and amorphous regions, known as α-relaxation and β-relaxation, respectively [59, 67]. Neat ENR-50, however, shows only one relaxation at 10^5 Hz, which corresponds to the segmental α-relaxation of ENR-50. In addition, a sharp increase in loss factor at low frequencies is observed for ENR-50 and PVDF/ENR-50 blends with and without BT particles, which is attributed to conduction loss. Furthermore, all blends show loss-factor peaks in the frequency range $10^4–10^7$ Hz, which correspond to a sharp decrease in permittivity at high frequency. It is anticipated that the loss-factor peaks and sharp decrease in permittivity correspond to segmental motions of PVDF and ENR-50 molecules. Therefore, BT successfully enhances the dielectric permittivity of both PVDF/ENR-50 blend compositions. The 80/20 blend exhibits the highest ε' because it combines a continuous, high-PVDF-content matrix with the strong polarization contribution of BT and the heterogeneous PVDF/ENR-50/BT interfaces. The 50/50 blend also shows substantial dielectric improvement, but its response is influenced more strongly by the BT-induced transformation to an ENR-50-continuous/PVDF-dispersed morphology. BT therefore acts simultaneously as a high-permittivity functional filler and a morphology-controlling component. Its net dielectric effect is governed by its intrinsic

ferroelectric response, selective localization, interfacial polarization, blend composition, and phase continuity.

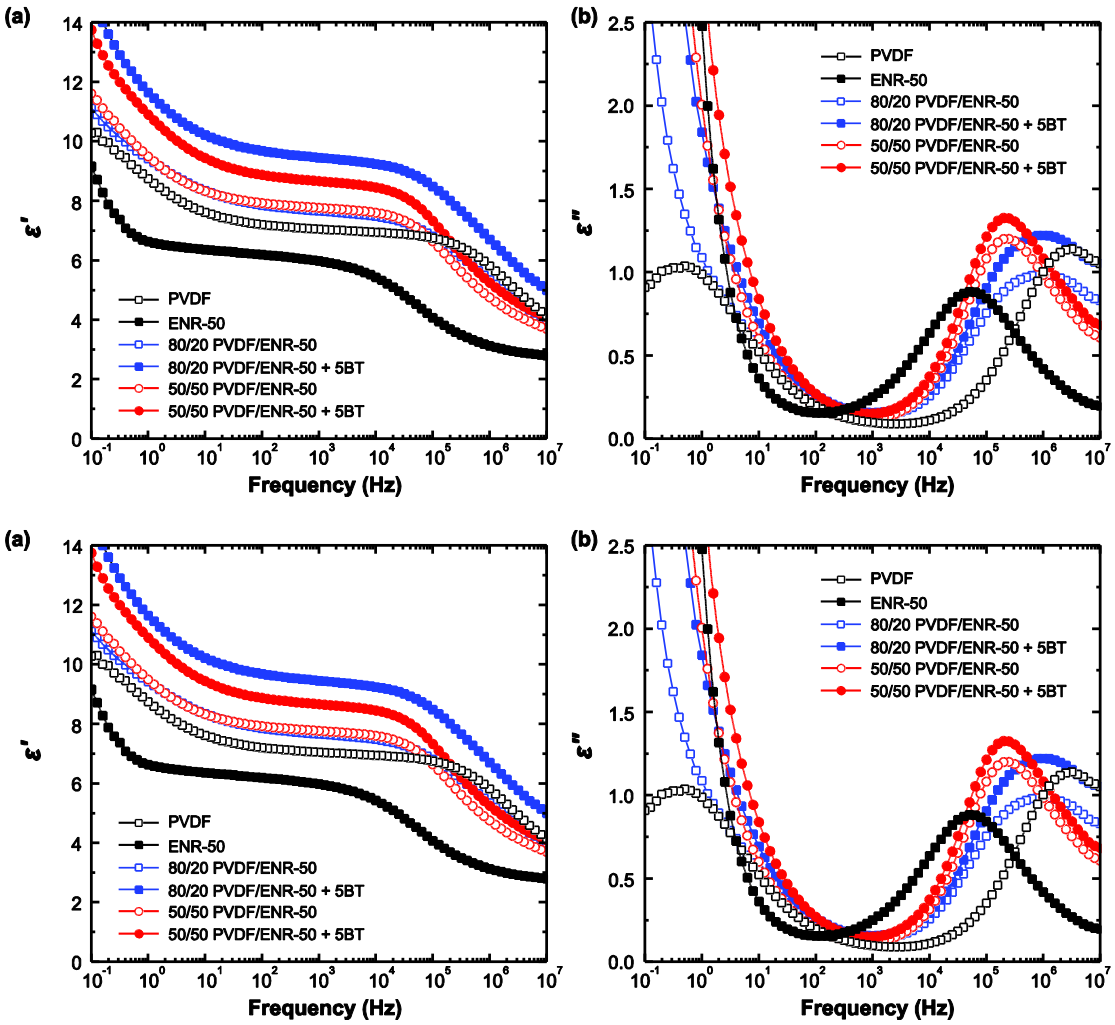


Figure 12. Frequency dependence of (a) dielectric permittivity (ε′) and (b) dielectric loss (ε″) at room temperature for the 80/20 and 50/50 PVDF/ENR-50 nonvulcanized blends without and with 5 vol% BT.

4. Conclusions

Non-vulcanized PVDF/ENR-50 blends were successfully prepared over a broad composition range to clarify the direct influence of blend composition and phase continuity

without interference from chemical crosslinking. The morphology evolved from a PVDF-continuous/ENR-50-dispersed structure at high PVDF contents to an apparent co-continuous region at 60/40–50/50, followed by an ENR-50-continuous/PVDF-dispersed structure at higher ENR-50 contents. Two phase-inversion boundaries were therefore identified: approximately between 70/30 and 60/40 and between 50/50 and 40/60 PVDF/ENR-50. This systematic identification addresses the gap left by previous studies that examined only limited blend ratios or dynamically vulcanized systems. The morphological transition governed the overall material performance. Increasing ENR-50 content reduced tensile stress, hardness, and storage modulus but markedly increased flexibility, damping, and elongation at break, which reached approximately 1000–2200% for ENR-50-rich blends. The 60/40 and 50/50 compositions provided the most useful balance between the load-bearing contribution of continuous or interconnected PVDF and the deformation capability of the continuous ENR-50 phase. PVDF crystallization was also composition-dependent: the crystallization temperature increased from 135.8 °C for neat PVDF to a maximum of 139.3 °C for the 50/50 blend, whereas the narrowest crystallization peak and highest PVDF-normalized crystallinity, 4.2 °C and 54.2%, respectively, were obtained for the 60/40 blend. At high ENR-50 contents, loss of PVDF continuity and spatial confinement reduced crystallinity to 43.7% for the 20/80 blend. The two DMA relaxation regions near −36 and −9 °C confirmed that the blends remained phase-separated but exhibited limited interfacial mixing or partial compatibility. Incorporation of 5 vol% BT demonstrated the principal novelty of this study: BT acted not only as a high-permittivity ceramic filler but also as a morphology-controlling component. BT preferentially localized in the ENR-50 phase and increased the average ENR-50 domain size in the 80/20 blend from approximately 6.5 to 11.4 μm while preserving the continuous PVDF matrix. In contrast, BT transformed the apparent co-continuous morphology of the 50/50 blend into an ENR-50-continuous/PVDF-dispersed structure. Consequently, the BT-filled 80/20 blend

retained comparatively high stiffness and exhibited the highest dielectric permittivity, whereas the BT-filled 50/50 blend showed lower tensile stress and rubbery-state modulus but greater deformation and damping. BT enhanced dielectric permittivity through its intrinsic ferroelectric response and additional polarization at the heterogeneous PVDF/ENR-50/BT interfaces, although this improvement was accompanied by increased dielectric loss, particularly at low frequencies. These findings demonstrate that blend composition, phase continuity, and selective filler localization can be used together to tailor stiffness, extensibility, damping, and dielectric response. The PVDF-rich BT-filled compositions are promising for flexible dielectric layers, low-voltage sensors, capacitive devices, and mechanically compliant electromechanical components, whereas the intermediate and ENR-50-rich compositions may be more suitable for flexible liners, cushioning materials, seals, and vibration-damping components. However, the present materials are more appropriate for low-load applications because the ENR-50 phase is not chemically crosslinked. Future work should determine the optimum BT loading, particle size, and surface treatment; improve particle dispersion and polymer–ceramic interfacial adhesion; and quantitatively confirm three-dimensional phase continuity using selective extraction, rheology, electrical continuity, or three-dimensional imaging. Dielectric breakdown strength, energy-storage density and efficiency, piezoelectric or actuation response, cyclic mechanical durability, creep, fatigue, thermal aging, and environmental stability should also be evaluated. Finally, introducing dynamic, reversible, or lightly crosslinked ENR-50 networks may improve dimensional stability and elastic recovery while retaining reprocessability and the morphology-dependent dielectric and damping advantages demonstrated in this study.

Acknowledgements

Financial support from the Thailand Research Fund through the Royal Golden Jubilee

Ph.D. Program (Grant No. PHD/0245/2549) to Dr. Charoen Nakason as principal researcher, and to Mr. Subhan Salaeh as the research assistant, as well as support from the French embassy in Thailand, are acknowledged. This work was also supported by the Higher Education Research Promotion and National Research University Project of Thailand by Office of the Higher Education Commission, and by Centre National de la Recherche Scientifique (CNRS) UMR 5223 “IMP@Lyon1”.

Author contributions

Subhan Salaeh: Data curation, Formal analysis, Investigation, Methodology, Validation, Visualization, Writing – original draft. Philippe Cassagnau: Methodology Resources, Supervision. Charoen Nakason: Conceptualization, Project administration, Resources, Supervision, Validation, Writing – review and editing.

Funding

This work was supported by the Thailand Research Fund through the Royal Golden Jubilee Ph.D. Program (Grant No. PHD/0245/2549)

Data availability

All the relevant data supporting the findings of this study are available within the manuscript.

Declarations

Conflict of interest The authors declare that they have no conflict of interest.

References

1. Higgins JS, Lipson JEG, White RP (2010) A simple approach to polymer mixture miscibility. Philos Trans A Math Phys Eng Sci 368(1914):1009-25. https://doi.org/10.1098/rsta.2009.0215

2. Koning C, Van DM, Pagnoulle C, Jérôme R (1998) Strategies for compatibilization of polymer blends. Prog Polym Sci 23:707–757. https://doi.org/10.1016/S0079-6700(97)00054-3

3. Pötschke P, Paul DR (2003) Formation of co-continuous structures in melt-mixed immiscible polymer blends. J Macromol Sci Part C 43:87–141. https://doi.org/10.1081/MC-120018022

4. Macosko CW (2000), Morphology development and control in immiscible polymer blends. Macromol Symp 149: 171-184. https://doi.org/10.1002/1521-3900(200001)149:1<171::AID-MASY171>3.0.CO;2-8

5. Zhou Y, Yu F, Deng H, Huang Y, Li G, Fu Q (2017) Morphology evolution of polymer blends under intense shear during high speed thin-wall injection molding. J Phys Chem B 121(25):6257-6270. https://doi.org/10.1021/acs.jpcb.7b03374

6. Jiang G, Wu H, Guo S (2010) Reinforcement of adhesion and development of morphology at polymer–polymer interface via reactive compatibilization: A review. Polym Eng Sci, 50:2273-2286. https://doi.org/10.1002/pen.21686

7. Antunes CF, Machado AV, van Duin M (2011) Morphology development and phase inversion during dynamic vulcanisation of EPDM/PP blends, Eur Polym J 47(7):1447-1459. https://doi.org/10.1016/j.eurpolymj.2011.04.005.

8. Puyvelde PV, Velankar S, Moldenaers P (2001) Rheology and morphology of compatibilized polymer blends. Curr Opin Colloid Interface Sci 6(5–6):457-463. https://doi.org/10.1016/S1359-0294(01)00113-3.

9. Fredrickson GH, Xie S, Edmund J, Le ML, Sun D, Grzetic DJ, Vigil DL Delaney KT, Chabinyc ML, Segalman RA (2022) Ionic compatibilization of polymers. ACS Polym Au 2(5):299-312. https://doi.org/10.1021/acspolymersau.2c00026.

10. Klonos PA, Lazaridou M, Samiotaki C, Kyritsis A, Bikiaris DN (2022) Dielectric and calorimetric study in renewable polymer blends based on poly(ethylene adipate) and poly(lactic acid) with microphase separation, Polymer 259:125329, https://doi.org/10.1016/j.polymer.2022.125329.

11. Banerjee R, Ray SS (2023) Role of rheology in morphology development and advanced processing of thermoplastic polymer materials: a review. ACS 8(31):27969-28001. https://doi.org/10.1021/acsomega.3c03310.

12. Colonna S, Han Z, Fina A (2018). Decoupled trends for electrical and thermal conductivity in phase-confined CNT co-continuous blends. Nanocomposites 4(3):80–86. https://doi.org/10.1080/20550324.2018.1503782

13. Galloway JA, Macosko CW (2004), Comparison of methods for the detection of cocontinuity in poly(ethylene oxide)/polystyrene blends. Polym Eng Sci 44:714-727. https://doi.org/10.1002/pen.20064

14. Harrats C, Groeninckx G (2004) Reactive processing of polymer blend using reactive compatibilization and dynamic crosslinking: phase morphology control and microstructure – property relations. In: Ciardelli F, Penczek S (eds) Modification and blending of synthetic and natural macromolecules. NATO Science Series, vol 175. Springer, Dordrecht. https://doi.org/10.1007/978-1-4020-2735-2_9

15. Ning N, Li S, Wu H, Tian H, Yao P, Hu G-H, Tian M, Zhang L (2018) Preparation, microstructure, and microstructure-properties relationship of thermoplastic vulcanizates (TPVs): A review. Prog Polym Sci 79:61-97. https://doi.org/10.1016/j.progpolymsci.2017.11.003.

16. Spontak RJ, Patel NP (2000) Thermoplastic elastomers: fundamentals and applications. Curr Opin Colloid Interface Sci 5(5–6):333-340. https://doi.org/10.1016/S1359-0294(00)00070-4.

17. Lehman N, Tuljittraporn A, Songtipya L, Uthaipan N, Sengloyluan K, Johns J, Nakaramontri Y, Kalkornsurapranee E (2022) Influence of non-rubber components on the properties of unvulcanized natural rubber from different clones. Polymers 14(9):1759. https://doi.org/10.3390/polym14091759

18. Wang Y, Liao L, Wang R, Yu H, Zheng T, Lian Y, Luo M, Liao S, Liu H, Peng Z (2023), Research of strain induced crystallization and tensile properties of vulcanized natural rubber based on crosslink densities. Ind Crops Prod 202:117070. https://doi.org/10.1016/j.indcrop.2023.117070.

19. Treitler JM, Saijun D, Phatcharasit K, Rattanapan S (2025) Novel compatibilization of nylon-12/natural rubber thermoplastic elastomers using hydroxyl telechelic natural rubber and natural fiber reinforcement. Express Polym Lett 19(12):1310-1319, 2025 DOI: 10.3144/expresspolymlett.2025.96

20. Salaeh S, Thitithammawong A, Banerjee SS (2024) A new strategy applying ternary blends of modified natural rubber with fluoroplastic and fluorocarbon elastomer for high-performance thermoplastic vulcanizate. Polym Test 140:108594. https://doi.org/10.1016/j.polymertesting.2024.108594.

21. Pei X, Hao Y, Shi y (2025) Controlled and expeditious synthesis of epoxidized natural rubber and stable latex modulated by cationic surfactants. J Polym Sci 63(22):4848–4859. https://doi.org/10.1002/pol.20250474.

22. Wang Z, Song H, Wang R, Zhang X, Yuan Q, Lu Y, Song W, Wu X, Hu G-H, Zhang L (2025). Effects of epoxidation degree on strain-induced crystallization and mechanical properties of epoxidized natural rubber. Polymer 333:128541, https://doi.org/10.1016/j.polymer.2025.128541.

23. Sarkawi SS, Aziz, CAK, Ismail NNI (2023) General compounding and properties of epoxidised natural rubber. In: Sarkawi SS, Rasdi, FRM, Charlotte V (eds) Epoxidised natural rubber. Springer, Singapore. https://doi.org/10.1007/978-981-19-8836-3_4

24. Zheng H, Yue D (2025) Lignin/epoxidized natural rubber compounds based on wet mixing: impact of epoxidation degree on the interface of compounds. Materials 18(16):3736. https://doi.org/10.3390/ma18163736

25. Song W, Wang Z, Wang M, Zhang G, Li F, Zhang X, Lu Y, Zhang L (2023) Comparative study of vulcanization system on strain-induced crystallization of epoxidized natural rubber, Polymer, 274:125911. https://doi.org/10.1016/j.polymer.2023.125911.

26. Nakason C, Narathichat M, Kummerlöwe C, Vennemann N (2013) Thermoplastic natural rubber based on polyamide-12 blended with various types of natural rubber: Effect of processing oils and plasticizer: Effect of processing oils and plasticizer. J Elastom Plast 45(1):47-75. https://doi.org/10.1177/0095244312445522

27. Norfarhana AS, Ilyas RA, Ngadi N, Sharma S, Sayed MM, El-Shafay AS, Nordin AH (2022) Natural fiber-reinforced thermoplastic enr/pvc composites as potential membrane technology in industrial wastewater treatment: A review. Polymers 14(12):2432. https://doi.org/10.3390/polym14122432

28. Srisuwanno T, Johns J, Bascucci C, Clemens F, Nakaramontri Y (2025) Effect of bio-based epoxidized natural rubber as a compatibilizer in thermoplastic polyurethane/natural rubber blends: Physical characterization and 3D printing behavior Express Polym Lett 19(10):1053-1072. https://doi.org/10.3144/expresspolymlett.2025.79

29. Huang J, Wu H, Wang X, Tan L, Xu W, Wang Q, Liang Y, Yu H, Liu Z, Xu B, Xiao S (2024) Using tannin as a biological curing agent to design fully bio-based epoxidized natural rubber/polylactic thermoplastic vulcanizates with mechanical robustness and multi-stimuli-responsive shape memory properties, International. Int J Biol Macromol 282(Part 4):137173. https://doi.org/10.1016/j.ijbiomac.2024.137173.

30. Kao-ian P, Banerjee SS, Salprima YS, Salaeh S (2024) Strengthened poly(vinylidene fluoride)/epoxidized natural rubber blend by a reactive compatibilizer based on an amino acid-modified fluorocarbon elastomer. Ind Eng Chem Res 63(15):6615-6631 https://doi.org/10.1021/acs.iecr.3c04672

31. Yu L, Yang D (2023) Enhanced electromechanical behaviours of epoxidized natural rubber composites via constructing non-covalent and covalent bonds by using tannic acid and Si747, Polymer, 277:125971. https://doi.org/10.1016/j.polymer.2023.125971.

32. Hu W, Wang C, Fei F, Wang R, Wang J, Tian H, Zhu Y, Zhang H (2025) Self-healing epoxidized natural rubber flexible sensors based on hydrogen bonding interactions. J Mater Chem C 13 (4):1824–1834. https://doi.org/10.1039/d4tc03214d

33. Concha VOC, Timóteo L, Duarte LAN Bahú JO, Munoz FL, Silva AP, Lodi L, Severino P, León-Pulido J, Souto EB (2024) Properties, characterization and biomedical applications of polyvinylidene fluoride (PVDF): a review. J Mater Sci 59: 14185–14204. https://doi.org/10.1007/s10853-024-10046-3

34. Costa CM, Cardoso VF, Martins P, Correia DM, Gonçalves R, Costa P, Correia V, Ribeiro C, Fernandes MM, Martins PM, Lanceros-Méndez S (2023) Smart and multifunctional materials based on electroactive poly(vinylidene fluoride): recent advances and opportunities in sensors, actuators, energy, environmental, and biomedical applications. Chem Rev 123(19):11392-11487. https://doi.org/10.1021/acs.chemrev.3c00196.

35. Ahbab N, Naz S, Xu T-B, Zhang S (2025) A comprehensive review of piezoelectric pvdf polymer fabrications and characteristics. Micromachines 16(4):386. https://doi.org/10.3390/mi16040386

36. Hedayati M, Taheri-Nassaj E, Yourdkhani A, Rasekh S, Sebastian T, Clemens FJ (2025). Dielectric properties and energy storage behavior of PVDF-based nanocomposites filled with BaTiO3 nanotubes and nanofibers: A comparative study. Ceram Int 51(20):31162-31175. https://doi.org/10.1016/j.ceramint.2025.04.304.

37. Padurariu L, Brunengo E, Canu G, Curecheriu LP, Conzatti L, Buscaglia MT, Stagnaro P, Mitoseriu L, Buscaglia V (2023) Role of microstructures in the dielectric properties of pvdf-based nanocomposites containing high-permittivity fillers for energy storage. ACS Appl Mater Interfaces 15 (10):13535–13544. https://doi.org/10.1021/acsami.2c23013

38. Bouhamed A, Missaoui S, Ayed BA, Attaoui A, Missaoui D, Jeder K, Guesmi N, Njeh A, Khemakhem H, Kanoun OA (2024) Comprehensive review of strategies toward efficient flexible piezoelectric polymer composites based on $BaTiO_3$ for Next-generation energy harvesting. Energies 17(16):4066. https://doi.org/10.3390/en17164066

39. Sun Q, Wang J, Sun H, He L, Zhang L, Mao P, Zhang X, Kang F, Wang Z, Kang R, Zhang L (2021) Simultaneously enhanced energy density and discharge efficiency of layer-structured nanocomposites by reasonably designing dielectric differences between BaTiO3@SiO2/PVDF layers and BNNSs/PVDF-PMMA layers, Compos-A: Appl Sci

Manuf 149:106546. https://doi.org/10.1016/j.compositesa.2021.106546.

40. Iida T, Hasegawa H, Yamaguchi M, Matsumura K, Hayakawa M, Tsugawa N (2025) Development of gradient structure in miscible PMMA/PVDF blends under temperature gradient, Polymer, 325:128298, https://doi.org/10.1016/j.polymer.2025.128298.
41. Tu R, Sodano HA (2023). Highly stretchable printed poly(vinylidene fluoride) sensors through the formation of a continuous elastomer phase. ACS Appl Mater Interfaces 15 (18):22320–22331. https://doi.org/10.1021/acsami.3c01168
42. Bertolini MC, Ramoa SDAS, Pereira ECL, Soares BG, Barra GMO, Pegoretti A (2023) Poly(vinylidene fluoride) and thermoplastic polyurethane composites filled with carbon black-polypyrrole for electromagnetic shielding applications. Polym Adv Technol 34(12):3838-3848. https://doi.org/10.1002/pat.6184
43. Salaeh S, Banda T, Pongdong V, Wießner S, Das A, Thitithammawong A (2018) Compatibilization of poly(vinylidene fluoride)/natural rubber blend by poly(methyl methacrylate) modified natural rubber. Eur Polym J 107:132-142, https://doi.org/10.1016/j.eurpolymj.2018.08.007.
44. Salaeh S, Nakason C, Boiteux G, Gain O, Cassagnau P (2013). Co-continuous phase structure and properties of poly(vinylidene fluoride)/epoxidized natural rubber blends. Adv Mater Res 626, 71–75. https://doi.org/10.4028/www.scientific.net/AMR.626.71
45. Salaeh S, Boiteux G, Gain O, Cassagnau P, Nakason C (2014). Dynamic mechanical and dielectric properties of poly(vinylidene fluoride) and epoxidized natural rubber blends. Adv Mater Res 844:97–100. https://doi.org/10.4028/www.scientific.net/AMR.844.97

46. Salaeh S, Boiteux G, Cassagnau P, Nakason C (2018) Thermoplastic vulcanizates based on poly(vinylidene fluoride)/epoxidized natural rubber blends: Effects of phenolic resin dosage and blend ratio. Mater Chem Phys 219:222–232. https://doi.org/10.1016/j.matchemphys.2018.08.029

47. Landis FA, March SR, Deivasagayam D, Mathers RT (2014) Crystallization of poly(vinylidene fluoride) in blends with poly(methyl methacrylate-co-methacrylic acid) copolymers. Macromol Chem Phys 215:153-162. https://doi.org/10.1002/macp.201300535

48. Willemse RC, Posthuma de Boer A, van Dam J, Gotsis AD (1988) Co-continuous morphologies in polymer blends: a new model. Polymer 39:5879–5887. https://doi.org/10.1016/S0032-3861(97)10200-2

49. Steinmann S, Gronski W, Friedrich C (2001). Cocontinuous polymer blends: influence of viscosity and elasticity ratios of the constituent polymers on phase inversion. Polymer 42:6619–6629. https://doi.org/10.1016/S0032-3861(01)00100-8

50. Wu S (1985) Phase structure and adhesion in polymer blends: A criterion for rubber toughening. Polymer 26:1855-1863. https://doi.org/10.1016/0032-3861(85)90015-1

51. Veenstra H, Verkooijen PCJ, van Lent BJJ, van Dam J, Posthuma de Boer A, Nijhof AHJ (2000) On the mechanical properties of co-continuous polymer blends: Experimental and modelling. Polymer 41:1817-1826. https://doi.org/10.1016/S0032-3861(99)00337-7

52. Kaesaman A, Sasdipan K, Nakason C (2026) Effect of epoxide content on interfacial interaction, morphology, and properties of non-vulcanized copolyester/epoxidized natural rubber blends. Polym. Bull. 83:505. https://doi.org/10.1007/s00289-026-06571-7

53. Xian W, Zhan Y-S, Maiti A, Saab AP, Li Y (2024) Filled elastomers: Mechanistic and physics-driven modeling and applications as smart materials. Polymers. 16(10):1387. https://doi.org/10.3390/polym16101387

54. Müller AJ, Michell RM, Lorenzo AT (2016) Isothermal crystallization kinetics of polymers. In: Guo Q (ed) Polymer morphology: principles, characterization, and processing; Wiley, New York.

55. Michell RM, Müller AJ (2016) Confined crystallization of polymeric materials. Prog. Polym Sci 54–55:183–213. https://doi.org/10.1016/j.progpolymsci.2015.10.007.

56. Toda A (2025). Crystallization kinetics, Avrami analysis, and fast-scanning DSC of polymers, Polymer 332:128522. https://doi.org/10.1016/j.polymer.2025.128522.

57. Meereboer NL, Terzić I, Saidi S, Merino DH, Loos K (2018) Nanoconfinement-induced β-phase formation inside poly(vinylidene fluoride)-based block copolymers ACS Macro Letters 7(7):863-867. https://doi.org/10.1021/acsmacrolett.8b00418

58. Ma W, Yuan H, Wang X (2014) The effect of chain structures on the crystallization behavior and membrane formation of poly(vinylidene fluoride) copolymers. Membranes 4(2):243-256. https://doi.org/10.3390/membranes4020243

59. Sencadas V, Lanceros-Méndez S, Serra SR, Balado AA, Ribelles JLG (2012) Relaxation dynamics of poly(vinylidene fluoride) studied by dynamical mechanical measurements and dielectric spectroscopy. Eur Phys J E 35:41 https://doi.org/10.1140/epje/i2012-12041-x

60. Dallaev R, Pisarenko T, Sobola D, Orudzhev F, Ramazanov S, Trčka T (2022) Brief review of pvdf properties and applications potential. Polymers14(22):4793. https://doi.org/10.3390/polym14224793.

61. Neidhöfer M, Beaume F, Ibos L, Bernès A, acabanne CL (2003). Structural evolution of PVDF during storage or annealing, Polymer, 45(5):1679-1688, https://doi.org/10.1016/j.polymer.2003.12.066.

62. Gomez-Menendez M, Stavropoulou VM, Asenjo-Sanz J, Pomposo JA, Verde-Sesto E, Arrese-Igor S, Maiz J (2026) Tuning segmental dynamics of PVDF in blends with linear precursors and single-chain nanoparticles: Insights from broadband dielectric spectroscopy. Polymer 347:129682. https://doi.org/10.1016/j.polymer.2026.129682.

63. El Mohajir B-E, Heymans N (2001). Changes in structural and mechanical behaviour of PVDF with processing and thermomechanical treatments. I. Change in structure. Polymer 42(13):5661-5667, https://doi.org/10.1016/S0032-3861(01)00064-7.

64. Lee JC, Litt M (2000). Glass transition temperature-composition relationship of oxyethylene copolymers with chloromethyl/(ethylthio)methyl, chloromethyl/(ethylsulfinyl)methyl, or chloromethyl/(ethylsulfonyl)methyl side groups. Polym J 32:228–233. https://doi.org/10.1295/polymj.32.228

65. Amoabeng D, Velankar SSA (2017) Composition–morphology map for particle-filled blends of immiscible polymers. Polymer 119:212–223. https://doi.org/10.1016/j.polymer.2017.05.022

66. Salaeh S, Nakason C, Boiteux G, Cassagnau P (2017). Dynamically cured poly(vinylidene fluoride)/epoxidized natural rubber blends filled with ferroelectric ceramic barium titanate,Compos - A: Appl Sci Manuf 93:107-116.

67. Sundararaj U, Macosko CW (1995) Drop breakup and coalescence in polymer blends: the effects of concentration and compatibilization. Macromolecules 28(8):2647-2657 DOI: 10.1021/ma00112a009

68. Fu S-Y, Feng X-Q, Lauke B, Mai Y-W (2008) Effects of particle size, particle/matrix interface adhesion and particle loading on mechanical properties of particulate–polymer composites. Compos B Eng 39(6): 933-961. https://doi.org/10.1016/j.compositesb.2008.01.002.

69. Plattier J, Benyahia L, Dorget M, Niepceron F, Tassin J-F (2015) Viscosity-induced filler localisation in immiscible polymer blends, Polymer 59:260-269. https://doi.org/10.1016/j.polymer.2014.12.044.

70. Kong M, Huang Y, Chen G, Yang Q, Li G (2011) Retarded relaxation and breakup of deformed PA6 droplets filled with nanosilica in PS matrix during annealing. Polymer 52(22):5231-5236, https://doi.org/10.1016/j.polymer.2011.08.052.

71. Xia X, Zhong Z, Weng GJ (2017) Maxwell–Wagner–Sillars mechanism in the frequency dependence of electrical conductivity and dielectric permittivity of graphene-polymer nanocomposites. Mech Mater 109:42-50. https://doi.org/10.1016/j.mechmat.2017.03.014.

72. Samet M, Kallel A, Serghei A (2022) Maxwell–Wagner–Sillars interfacial polarization in dielectric spectra of composite materials: Scaling laws and applications. J Compos Mater 56(20): 3197–3217. https://doi.org/10.1177/00219983221090629

73. Lin X, Fan L, Ren D, Jiao Z, Coates PD, Yang W, Enhanced dielectric properties of immiscible poly (vinylidene fluoride)/low density polyethylene blends by inducing multilayered and orientated structures. Compos B Eng 114:58-68. https://doi.org/10.1016/j.compositesb.2017.01.065.

74. Han H, Voisin C. Guillemet-Fritsch S, Dufour P, Tenailleau C, Turner C, Nino JC (2013) Origin of colossal permittivity in $BaTiO_3$ via broadband dielectric spectroscopy. J Appl Phys 113 (2): 024102. https://doi.org/10.1063/1.4774099

75. Liang Y, Sun W, Li T, Chen Y, Cheng Y, Zhang L (2023) All organic polymer dielectrics for high-temperature energy storage from the classification of heat-resistant insulation grades. J Polym Sci 61(22):2777. https://doi.org/10.1002/pol.20230334